Polyamines regulate cell fate by altering the accessibility of histone tails.

Maya Emmons-Bell[1,2], Abby Sundquist[1,*], Megan R. Rabon[1,3,*], Grace Forsyth[4], Sylvie Oldeman[5], Shine Ayyapan[6], Angeliki Gardikioti[1], Roshni de Souza[1], Jonathan Coene[7], Maryam H. Kamel[3,8,9], Harrison A. Fuchs[6], Varun S. Sudunagunta[10], Edna M. Stewart[11], Steven Verhelst[7], Joanna Smeeton[3,8,9], Aaron D. Viny[3,8,12], Catherine A. Musselman[6], Juan-Manuel Schvartzman[1,12,13]

[1]Columbia University, Herbert Irving Comprehensive Cancer Center, New York, NY, USA; [2]Yale School of Medicine, Boyer Center for Molecular Medicine, New Haven, CT; [3]Department of Genetics and Development, Columbia University Irving Medical Center, Columbia University, New York, NY, USA; [4]Weill Cornell Medical College, New York, NY, USA; [5]Barnard College, New York, NY, USA; [6]Department of Biochemistry and Molecular Genetics, University of Colorado Anschutz Medical Campus, Aurora, CO, USA; [7]University of Leuven, Cellular and Molecular Medicine, Leuven, Belgium; [8]Columbia Stem Cell Initiative, [9]Department of Rehabilitation and Regenerative Medicine, [10]Columbia University Vagelos College of Physicians and Surgeons; [11]Department of Biochemical Engineering, Columbia University; [12]Columbia University Irving Medical Center, Department of Medicine, Division of Hematology/Oncology, New York, NY, USA.

[13]Corresponding author

* These authors contributed equally.

Abstract

Polyamines are polycationic alkyl-amines abundant in proliferating stem and cancer cells. How these metabolites influence numerous cellular processes remains unclear. Here we show that polyamine levels decrease during differentiation and that inhibiting polyamine synthesis leads to a differentiated-like cell state. Polyamines are enriched in the nucleus, where their loss drives changes in chromatin accessibility and histone post-translational modifications. Polyamines interact electrostatically with DNA on the nucleosome core, freeing histone tails to conformations accessible to chromatin-modifying enzymes. Consistent with their role in

increasing histone-tail accessibility, polyamines are able to replace MYC's role in reprogramming to pluripotency. These data reveal a mechanism by which an abundant metabolite influences chromatin structure and function in a direct but sequence independent manner, facilitating chromatin remodeling during reprogramming and limiting it during fate commitment.

Introduction

The polyamines putrescine, spermidine and spermine are polycationic (positively-charged) alkyl-amines present at high concentrations in eukaryotic cells[1,2]. Polyamines are synthesized by decarboxylation of the amino acid ornithine by the enzyme ornithine decarboxylase (ODC1) (Fig. 1A). At approximately 1 mM, polyamine concentration in proliferating cells is within the range of abundant amino acids like glutamine[2,3]. Polyamine biosynthesis is upregulated in proliferating cells, while its inhibition results in cell cycle arrest[4–6]. In some cases, this arrest resembles terminal differentiation[7–9]. Consistent with proliferating cells requiring high levels of polyamines, ODC1 is a top transcriptional target of the transcription factor MYC[10], and upregulation of ODC1 is required for the transforming effects of MYC[11,12]. ODC1 is an irreversible enzyme in metazoans, therefore cells cannot normally recover carbon or nitrogen from existing polyamine pools. Thus, proliferating cells invest a significant fraction of critical nutrients (e.g. glutamine and arginine) in the irreversible production of polyamines, yet their biological role is poorly understood.

Mechanistically, polyamines have been shown to perform multiple biological functions, including participating in the post-translational modification of the translation initiation factor eIF5A[13,14] and regulating the activity of inwardly rectifying potassium channels[15]. Earlier work has also shown that polyamines interact with negatively-charged macromolecules like DNA and RNA. This interaction with DNA can alter chromatin accessibility, nucleosome condensation[16,17] , and increase transcriptional efficiency *in vitro*[16,18–21], but whether and how this occurs *in vivo* is unknown. Here we show that polyamines are enriched in the nucleus, where their interaction with chromatin enables increased accessibility of the histone tail to chromatin-modifying enzymes. These interactions are critical for the regulation of cell state. By decreasing polyamine levels, differentiating cells limit noisy chromatin dynamics, enabling faithful lineage commitment. Conversely, increasing intracellular polyamine concentrations facilitates lineage plasticity and reprogramming. Thus, polyamines alter the flexibility of chromatin landscapes in an enzyme- and sequence-agnostic manner, facilitating a broad diversity of cell state transitions.

56

57 **Results**

58 **Polyamine biosynthesis is decreased during differentiation.**

59 Since polyamine content is highest in undifferentiated cells, we wondered if polyamine metabolism is regulated
60 during differentiation. To explore transcriptional regulation of polyamine biosynthesis, we mined published
61 RNAseq datasets in diverse models of differentiation. Across many models (3T3L1 cells during adipocyte
62 differentiation, 10T1/2 cells during osteoblast differentiation, human chondrocyte tissue samples during early
63 development, human embryonic stem cells during neuronal differentiation, C2C12 cells during myotube
64 differentiation, and human hematopoietic cells), we found that ornithine decarboxylase (ODC1) expression
65 decreased as cells underwent fate commitment (Fig. 1B and Fig. S1A-H). Expression of spermidine synthase
66 was also decreased during differentiation, but spermine synthase expression was not clearly correlated with
67 differentiation state in every model (Fig. S1C-H). We next asked if cellular polyamine content similarly
68 decreased as cells differentiated. We used two well established models of differentiation: K562 myelogenous
69 leukemia cells differentiated into erythrocytes, and murine myoblasts (C2C12 cells) differentiated into
70 myotubes. We validated induction of differentiation by western blot for lineage markers (Fig. 1C). To quantify
71 cellular polyamine content, we used an optimized protocol for polyamine extraction and derivatization for gas
72 chromatography mass spectrometry (GC-MS; K562) or LC-MS (C2C12; See Materials and Methods)[22]. In both
73 models, we found that levels of polyamines decreased during differentiation (Fig. 1D and E) and remained low
74 as cells continued differentiating. This was especially the case in K562 cells, where levels of all polyamine
75 species decreased markedly during differentiation (Fig. 1D). For the myoblast to myotube model (C2C12),
76 overall polyamine levels were lower, requiring more sensitive LCMS analysis, and putrescine levels showed a
77 clear sustained decrease during differentiation, though this decrease was not as marked for spermidine and
78 spermine (Fig. 1E). Finally, we mined a published metabolomics data set collected over the first ninety-six hours
79 of zebrafish development and found that putrescine and spermidine levels increased for 48h after fertilization,
80 then decreased as cells began to differentiate (Fig. S1I and Fig. S1J; N.B. spermine abundance was not

reported). These data demonstrate that across multiple models and at both the transcriptional and metabolite-levels, polyamine levels decrease during lineage commitment.

Polyamine depletion induces a differentiated-like cell state.

We next asked if polyamine depletion might play a causative role during differentiation. To test this, we depleted cells of polyamines and assessed their differentiation states. We used CRISPR-Cas9 to genetically ablate ODC1 in 10T1/2 cells, a murine mesenchymal progenitor cell line with multipotent potential[23]. We outgrew single cell clones in the presence of exogenous putrescine (Fig. S2A), and validated the effect of ODC1 knockout on polyamine content with GC-MS. The abundance of all three polyamine species was decreased in knockout cells (Fig. 2B, Fig. S2B). We also targeted ODC1 pharmacologically by treating cells with the irreversible ODC1 inhibitor di-fluoro-methyl-ornithine (DFMO), which decreased the abundance of all three polyamine species to a similar extent as ODC1 knockout (Fig. S2C).

Polyamines are known to be required for cell proliferation[4,24]. Consistent with this, DFMO-treated and ODC1 knockout cells failed to proliferate following three days of polyamine depletion (Fig. 2A). We did not observe decreases in cell number or viability (Fig. S2D) which would indicate widespread cell death, suggesting that the effect of polyamine depletion is cytostatic. EdU incorporation and cell cycle analysis by flow cytometry showed that polyamine depleted cells were specifically arrested in G1 (Fig. S2E). We were able to rescue the cytostatic effect of polyamine depletion in ODC1 knockout cells by supplementing media with 0.5 mM putrescine, validating enzymatic loss of function and indicating that knockout cells behaved like putrescine auxotrophs (Fig. 2A).

To our surprise, polyamine depletion resulted in changes in morphology in 10T1/2 cells. While wild-type 10T1/2 cells are normally cuboidal in shape, ODC1 knockout and DFMO-treated cells became elongated and spindly (Fig. 2C). The combination of cell cycle arrest in G1 and changes in morphology suggested that polyamine-

106 depleted cells might be undergoing a differentiation-like change in cell state. To explore whether polyamine
107 depletion was leading to differentiation, we carried out RNAseq on control and ODC1 knockout cells treated
108 with DFMO or exogenous putrescine, grouped the cells according to low or high polyamine content as assessed
109 by GC-MS, and performed differential gene expression analysis (Fig. 2D). Genes upregulated in polyamine-
110 depleted samples were involved in the regulation of diverse cell differentiation outcomes, multicellular
111 development, and intracellular signal transduction (Fig. 2E, top terms shown in Fig. S2F). Conversely, gene sets
112 down-regulated in polyamine-depleted cells were involved in cell cycle regulation (Fig. 2E, top terms shown in
113 Fig. S2G), agreeing with the cytostatic effect of polyamine depletion. Critically, polyamine depletion did not
114 lead to upregulation of genes associated with any one lineage, suggesting that polyamine depletion is not
115 inducing differentiation on its own, but rather promoting a "differentiation-like" or "differentiation-primed" cell
116 state.
117
118 A common feature of terminal differentiation is irreversible exit from the cell cycle. To explore whether the
119 arrest in G1 observed in polyamine-depleted cells was reversible, we treated cells with DFMO for three days,
120 then allowed them to recover for three days in media without drug. Polyamine-depleted cells did not resume
121 proliferation after drug washout (Fig. 2F). Thus, DFMO treatment induces a stable cell state change which is not
122 reversed when ODC1 function is restored. Taken together, these data suggest that polyamine depletion pushes
123 cells towards a more differentiated phenotype.
124
125 To test whether polyamine depletion induces differentiation in other contexts, we treated a panel of cell lines
126 with DFMO and assessed expression of lineage commitment markers by western blot. In 10T1/2 cells cultured in
127 chondrocyte differentiation media, DFMO treatment either 24 hours before or at the onset of differentiation
128 increased differentiation marker expression (Fig. 2G). However, DFMO had a negative effect on differentiation
129 if present once the differentiation process was underway. The multipotent nature of c10T1/2 cells enabled us to
130 probe whether differentiation into other lineages was similarly enhanced by polyamine depletion. As opposed

131 to enhancing chondrocyte differentiation, polyamine depletion with DFMO impaired adipocyte differentiation
132 (Fig. S2H). Polyamine depletion was also able to enhance differentiation of C2C12 myoblasts into myotubes;
133 DFMO treatment during the myoblast stage was able to prime differentiation, but impaired differentiation if
134 added during the final stages (Fig. 2G). As opposed to these non-transformed models of differentiation, in
135 three cancer cell lines tested (SK-N-BE(2) neuroblastoma, COLO858 melanoma, and K562 acute myeloid
136 leukemia) polyamine depletion resulted in decreased proliferation (Fig. S3A) and up-regulation of markers of
137 differentiation (Fig. 2G). Thus, when polyamines are depleted, non-transformed progenitors are primed for
138 increased differentiation towards a defined lineage and, in the case of a multipotent progenitor, away from an
139 alternative lineage as seen for adipocytes. Conversely, upon polyamine depletion, transformed cells are pushed
140 towards a differentiation-like state defined by their cell of origin. These data suggest that polyamine depletion
141 is not merely a consequence of lineage commitment, as experimental depletion is sufficient to drive cells
142 towards a more differentiated phenotype.
143
144 Polyamines are known to contribute to translational homeostasis through spermidine's role as a substrate for
145 eIF5a hypusination[13,14]. Hypusinated eIF5a facilitates the translation elongation and termination of polyproline-
146 rich and tripeptide repeat-containing proteins[25–27], and it has been suggested that polyamines impact growth
147 and lineage fidelity through their regulation of hypusination[28]. To investigate whether polyamine-depleted
148 10T1/2 cells were undergoing proteotoxic stress as a result of impaired translation, we pulsed cells with the
149 puromycin analogue O-propargyl-puromycin (OPP) and quantified global translation by flow cytometry. We did
150 not observe changes in bulk translation following depletion or addition of polyamines (Fig. S3B-C), nor did we
151 observe induction of phosphorylated eIF2a, a readout of the integrated stress response (Fig. S3D)[29]. To explore
152 the impact of hypusination on differentiation, we pharmacologically inhibited deoxyhypusine synthase (DHPS),
153 the enzyme responsible for forming the first intermediate deoxyhypusine residue on eIF5a. We validated
154 decreased hypusine levels following DHPS inhibition by western blot. Markers of differentiation either

155 decreased or did not change (Fig. S3E) after DHPS inhibition. These data suggest that the differentiation
156 phenotypes observed after polyamine depletion are not due to impaired hypusination.
157
158 **Polyamines are enriched in the nucleus.**
159 Subcellular compartmentalization of metabolites can restrict the effects of small molecules to specific parts of
160 a cell, even in the absence of membrane-bound organelles[30,31]. We reasoned that identifying where polyamines
161 were concentrated in cells might help illuminate their mechanism of action. Resolving subcellular localization of
162 metabolites by mass spectrometry is limited by the spatial resolution of MALDI (Matrix-Assisted Laser
163 Desorption/Ionization)[32], so we set out to identify an alternative imaging-based approach. We synthesized a
164 clickable putrescine probe consisting of putrescine with an azide group that can be covalently bound to a
165 fluorophore-alkyne label *in vitro* or *in vivo* (Fig. 3A). We treated live cells with the un-clicked probe, fixed,
166 permeabilized and performed click-chemistry to a fluorophore alkyne, and then imaged cells using confocal
167 microscopy. We did not observe any fluorescence signal when cells were exposed to the probe without an
168 alkyne fluorophore (Fig. S4A). Imaging after clicking the probe to a fluorophore revealed stark nuclear
169 localization in 10T1/2 cells (Fig. 3B). DFMO treatment of cells prior to incubation in polyamine probe increased
170 probe signal, presumably due to upregulation of polyamine transporters[33–35] . Similar effects were seen in ODC1
171 knockout 10T1/2 cells when grown in the absence of exogenous putrescine (Fig. S4B). Nuclear probe
172 localization was also observed with spermidine and spermine probes (Fig. 3C and Fig. 3D), and in RPE-1 and U-2
173 OS cells (Fig. S4D and Fig. S4E). Critically, incubation in D-alanine and L-ornithine azide probes did not reveal
174 nuclear localization, confirming that nuclear localization is a property unique to polyamines (Fig. S4A). To
175 determine if polyamines are primarily associated with chromatin (DNA and protein), or RNA species, we
176 incubated cells in the putrescine probe, and then treated cells with RNAse. Following RNAse treatment, cells
177 were washed thoroughly and imaged. Nuclear probe localization was observed regardless of RNAse treatment
178 (Fig. S4F, suggesting that polyamines are primarily associated with chromatin in the nucleus. To validate our
179 localization data *in vivo*, we manually dechorionated zebrafish embryos at the four-cell stage and exposed them

180 to the putrescine probe for two hours, then fixed, permeabilized, and performed click chemistry. The putrescine
181 probe again concentrated in nuclei, especially at the nuclear periphery (Fig. S4G). Taken together, these data
182 suggest that all three polyamine species are enriched in the nucleus, where they primarily associate with
183 chromatin.
184
185 **Polyamines increase the activity of diverse histone-modifying enzymes.**
186 Polyamines have been reported to alter DNA/DNA and DNA/protein interactions[36,37]. Given their nuclear
187 localization and the effects of polyamine depletion on differentiation, we set out to explore the impact of
188 polyamine depletion on chromatin. We first profiled chromatin accessibility broadly by performing micrococcal
189 nuclease (MNase) digestions on wildtype and ODC1 knockout 10T1/2 cells and quantifying the abundance of
190 mononucleosome fragments. Mononucleosome abundance was increased in ODC1 knockout cells (Fig. S5A),
191 suggesting that global chromatin accessibility increases upon polyamine depletion. To determine the specificity
192 of this change in chromatin accessibility, we performed ATACseq (Assay for Transposase-Accessible Chromatin
193 using sequencing) on 10T1/2 cells treated with DFMO or putrescine (Fig. 4A and Fig. S5B). Addition of
194 putrescine had minimal effects on chromatin accessibility, but polyamine depletion resulted in thousands of
195 regions of chromatin with either increased or decreased accessibility (Fig. 4A, Fig. S5C, samples normalized to
196 E. coli spike-in DNA). As we had seen with MNAse treatment, and consistent with earlier reports[21], we noticed
197 an overall increase in chromatin accessibility in DFMO-treated samples. At a more granular level, genes with
198 increased accessibility in transcriptional start sites following polyamine depletion were associated with the
199 regulation of anatomical structure size, morphogenesis, and cell adhesion (Fig. S5D), and de novo motif
200 enrichment analysis revealed binding sites for transcription factors known to coordinate lineage and responses
201 to diverse stressors (Fig. S5E). Together with our transcriptomic data, these results suggest that polyamine
202 depletion initiates a concerted rewiring of epigenetic and transcriptional landscapes, pushing cells towards a
203 more differentiated state.
204

205 Changes in chromatin accessibility are coordinated in part by enzymes that deposit modifications on histone
206 tails. To characterize histone tail modifications following polyamine depletion, we assessed the levels of a panel
207 of histone modifications by western blot, finding that some modifications increased, some decreased, and
208 some were unaltered (Fig. S5F). These changes were not due to the cytostatic effects of polyamine depletion,
209 as arresting cells in G1 with palbociclib did not induce changes in H3K18ac or H3K9me2 (Fig. S5G). Additionally,
210 we did not observe changes in global DNA 5mC content (Fig. S5H). We next wanted to understand how
211 polyamine depletion might alter histone tail modifications. A challenge of interpreting changes to bulk histone
212 modifications is that they are the sum of the activities of both writer and eraser enzymes. Therefore, we set out
213 tease apart the effect of polyamine depletion on different classes of histone-modifying enzymes. We exposed
214 10T1/2 and SK-N-BE(2) cells to inhibitors of histone acetyltransferases (JG2016, HATi) or histone deacetylases
215 (Vorinostat, HDACi) and depleted polyamines with DFMO. We reasoned that DFMO treatment in the context of
216 histone writer inhibition (HATi) would allow us to assess the impact of polyamine depletion on histone
217 deacetylase activity. HATi treatment decreased histone acetylation, reflecting the accumulated activity of
218 deacetylases (Fig. 4B). Polyamine depletion in the presence of histone acetyltransferase inhibition attenuated
219 this decrease, suggesting that polyamine depletion decreases the activity of histone deacetylase enzymes. The
220 same effect was seen after inhibition of deacetylases – increased acetylation following HDACi treatment was
221 decreased by concomitant polyamine depletion – as well as methyltransferase and demethylase inhibition, to
222 varying extents in the two cell lines tested (non-transformed 10T1/2 cells and transformed SK-NE-B(2) cells)
223 (Fig. S5I). This data suggests that polyamine depletion decreases the activity of diverse classes of histone-
224 modifying enzymes.
225
226 To directly query the impact of polyamines on histone-modifying enzymes, we performed *in vitro* histone
227 modification reactions with purified histone-modifying enzymes, cognate substrates, recombinant
228 nucleosomes, and polyamines. These assays have successfully demonstrated the role of metabolites in histone-
229 modifying enzyme activity[38]. As we observed decreased activity of histone methyltransferases,

230 acetyltransferases, demethylases and deacetylases in polyamine depleted cells, we performed *in vitro* reactions
231 with members of each of these four distinct enzyme classes in the presence of increasing polyamines, using the
232 histone modifications detected by western blotting as a read-out of catalytic activity. Spermine and, to a lesser
233 extent, spermidine increased the catalytic activity of the H3K9 histone-methyltransferase (HMT) G9a on
234 nucleosome substrates (Fig. 4C) while putrescine had little effect. Given the electrostatic charge relationship of
235 the different species (putrescine, 2+; spermidine, 3+; spermine, 4+), we wondered whether the increased
236 efficiency of spermine was related to its higher charge content. However, even with concentrations of
237 putrescine and spermidine that matched the charge concentration of spermine, spermine had the largest effect
238 on increasing G9a activity (Fig. 4D). To determine whether the effect of spermidine and spermine on G9a
239 methyl-transferase activity was dependent on an interaction of the polyamine with the nucleosome substrate
240 or the enzyme itself, we repeated the methyl-transferase reaction with purified histone H3. In this case, none of
241 the polyamines had any effect on catalytic activity (Fig. 4E). These results show that spermine, and to a lesser
242 extent, spermidine, can increase the ability of G9a to methylate histone H3 in the context of the nucleosome.
243
244 We next turned to evaluating the effects of polyamines on other histone-modifying enzymes. Spermine and
245 spermidine were also able to increase the efficiency of the histone acetyl-transferase (HAT) GCN5 on
246 nucleosome substrates (Fig. 4F). This effect was independent of charge (Fig. S5J) and was not seen when
247 histone H3, as opposed to intact nucleosomes, was provided as a substrate (Fig. S5K). To evaluate the effect of
248 polyamines on histone demethylation (KDM) activity, we incubated recombinant KDM4A, a Histone H3
249 K9me2/3 demethylase, with recombinant H3K9me3-modified nucleosomes. Again, spermine increased the
250 efficiency of H3K9me2/3 demethylation by KDM4A (Fig. 4G), in agreement with our *in vivo* results. Neither
251 putrescine nor spermidine increased the efficiency of this reaction. As shown for the histone writers G9a and
252 GCN5, the polyamine-specific increase in catalytic activity required intact nucleosomes, as they were not seen
253 with purified histone H3 (Fig. S5L). Finally, we evaluated the effect of polyamines on the catalytic activity of the
254 histone deacetylase SIRT6. In this case, neither individual polyamines nor a pool of polyamines was able to

increase the efficiency of acetylated H3 deacetylation in nucleosomes (Fig. 4H) or free histone H3 (Fig. S5M). These data suggest that spermine, to a lesser extent spermidine, and a pool of polyamines, can increase the catalytic activity of multiple subclasses of histone-modifying enzymes on nucleosome substrates but not free histone protein.

Polyamines increase the accessibility of the histone tail in the context of the nucleosome.

Deuterium exchange mass spectrometry has shown that histone tails are solvent protected, likely due to their electrostatic interactions with the DNA backbone[39]. This interaction has also been observed by NMR analysis[40–42]. To serve as substrates of enzymatic activity, polycationic histone tails must dissociate from negatively charged nucleosomal gyre DNA. We hypothesized that this dissociation was favored by polyamines, which would bind electrostatically to the DNA backbone and allow the histone tail to become freely available to diverse classes of histone-modifying enzymes. This model would explain why in our *in vitro* catalytic assays, polyamines only improved enzymatic activity when intact nucleosomes, rather than free histone H3, were the substrate. Importantly, we did not find evidence that polyamines at the concentrations used in our *in vitro* assays could denature DNA from the nucleosome core (Fig. S5N)[43]. Another prediction of this model is that as opposed to modifications of the relatively unstructured histone tail, modifications to the core histone particle, like histone H3K79 di-methylation catalyzed by the enzyme DOT1L, would not be impacted by polyamines. To test this, we treated 10T1/2 cells with DFMO alone or in combination with EPZ5676, an inhibitor of DOT1L[44], and found that H3K79me2 levels were unchanged (Fig. S5O). We also performed *in vitro* histone methylation reactions with recombinant DOT1L protein and found that enzymatic activity was unaffected by addition of polyamines (Fig. S5P).

To further characterize how polyamines affect tail accessibility in nucleosomes, we performed *in vitro* trypsin digestion assays[45]. In a time course of nucleosome digestion in vehicle- and spermidine- incubated reactions, spermidine increased the ability of trypsin to degrade the largest molecular weight band corresponding to

280 intact H3 histone (Fig. 5A and Fig. S6A). Spermine was also able to increase the ability of trypsin to digest
281 nucleosomal substrates, though in this case efficiency was more clearly demonstrated in the disappearance of
282 intermediate digestion products (Fig. 5B and Fig. S6A). A combination of all three natural polyamines was
283 similarly able to increase the efficiency of trypsin digestion of nucleosomal histones (Fig. S6B). As we had seen
284 for the catalytic assays with chromatin-modifying enzymes, none of the polyamines had any effect on the
285 ability of trypsin to digest recombinant free histone H3 (Fig. S6C). These results support a model whereby
286 polyamines increase the accessibility of the histone tail in the context of an intact nucleosome.
287
288 We next wanted to probe the structural changes that polyamines have on histone tail conformational
289 dynamics, as suggested by the *in vitro* enzymatic and trypsin tail digestion assays. Previous NMR studies have
290 shown that H3 tails are associated with DNA in the context of nucleosomes, forming what is termed a fuzzy
291 complex that is inhibitory to binding and can be regulated by histone post-translational modifications and
292 nucleosome composition[41,42,45–47]. To test if spermidine can alter the conformational ensemble of the H3 tail, we
293 performed chemical shift perturbation (CSP) experiments on a nucleosome core particle (NCP) in which H3 was
294 ^{15}N-labelled (^{15}N-H3-NCP) (Fig. S6D-E). With this labeling scheme, H3 tails are observable within the context of
295 the nucleosome. We collected ^{1}H, ^{15}N heteronuclear single quantum coherence (^{1}H, ^{15}N-HSQC) spectra on the
296 ^{15}N-H3-NCP in the absence and presence of spermidine (Fig. 5C-D and Fig. S6F). In the presence of spermidine
297 we observed CSPs consistent with an altered H3 tail conformational ensemble. These CSPs were observable
298 across the entire H3 tail, indicating that all residues are affected by spermidine. Notably, the direction of the
299 CSPs is consistent with previously observed CSPs seen upon addition of increasing monovalent or divalent salt
300 concentrations[42] which are known to enhance the accessibility of the H3 tail. We also carried out chemical shift
301 perturbations on a nucleosome core particle in the absence and presence of spermine (Fig. 5C-D and Fig. S6F).
302 In this case, we observed greater CSPs overall as compared to spermidine, but also saw these concentrated in
303 two regions: a smaller region closer to the N-terminus comprising H3 residues 3-8 and a larger region
304 encompassing H3 residues 19-29. To assess how spermine and spermidine alter the conformational dynamics

305 of the H3 tails we carried out ^{15}N-relaxation experiments and calculated the amino acid specific correlation
306 times (tC), which report on the overall mobility of each amino acid. Notably, spermidine led to a consistent
307 decrease in tC for residues 5-29, indicating an increase in the conformational dynamics of the majority of the H3
308 tail. While spermine also led to an increase in conformational dynamics, the effects were more localized,
309 affecting residues 3-11 and 15-21. Together, these data reveal that spermine and spermidine alter both the
310 conformational ensemble and dynamics of the H3 tails but in a manner specific to the polyamine. These *in vitro*
311 experiments provide orthogonal support for a model where polyamines change the conformational ensemble
312 of the H3 tail, likely by directly associating with the nucleosomal DNA to free and increase tail accessibility.
313

314 **Exogenous polyamines facilitate reprogramming.**

315 We have so far shown that polyamine depletion induces a lineage primed cell state by altering the ability of
316 histone-modifying enzymes to access histone tails. We wondered if exogenous polyamines might increase
317 chromatin dynamics and facilitate reprogramming of terminally differentiated cells. Supporting this, though
318 cells pre-treated with DFMO for three days did not re-initiate proliferation after removal of drug, they did
319 proliferate if media was supplemented with excess putrescine (Fig. 2F). ODC1 is a direct transcriptional target
320 of c-Myc, one of the four Yamanaka reprogramming factors[48]. We hypothesized that the role of c-Myc during
321 reprogramming might be in part to increase polyamine biosynthesis, thereby facilitating the chromatin
322 remodeling necessary for de-differentiation. To test this, we reprogrammed mouse embryonic fibroblasts
323 expressing an Oct4-GFP reporter by doxycycline-inducible expression of either three (Oct4, Sox2, and Klf4;
324 OSK) or four (Oct4, Sox2, Klf4, and Myc; OSKM) Yamanaka reprogramming factors for 12 days in the presence
325 of DFMO or putrescine. We assayed stable reprogramming efficiency by withdrawing cells from doxycycline for
326 four days, then quantifying Oct4-GFP expression and colony number (Fig. 5A-B). Reprogramming with OSK
327 resulted in low reprogramming efficiency with a small population of Oct4-expressing cells, while OSKM
328 expression led to reprogramming efficiencies comparable to previous reports[49,50]. Treatment of MYC-less OSK-
329 expressing cells with putrescine increased Oct4-GFP reporter expression and reprogramming efficiency nearly

330 to the levels of OSKM-reprogrammed fibroblasts (Fig. 5B-D), while DFMO treatment ablated reprogramming
331 capacity in OSK- or OSKM-expressing cells. These data show that a primary role of c-Myc during
332 reprogramming is its ability to increase polyamine biosynthesis.
333
334 **Exogenous polyamines can rescue the effects of losing histone tail acetylation.**
335 To determine whether the phenotypic consequences of increasing or decreasing polyamines were mediated by
336 their effects on histone tail accessibility, we focused on histone acetylation. Histone tail acetylation has been
337 thought to mediate effects on chromatin function and gene expression by increasing tail accessibility[41,51–53] .
338 Consistent with this, reprogramming from pluripotency is enhanced by histone deacetylase inhibitors[54,55] and
339 inhibition of histone acetylation inhibits reprogramming[56]. Given that inhibiting HATs reduces histone tail
340 accessibility, we reasoned that if exogenous polyamines could rescue phenotypes that result from acetyl-
341 transferase inhibition, it would suggest that polyamines exert their effects primarily through enhancing histone
342 tail accessibility, rather than through alternative mechanisms (e.g. protein translation or chromatin
343 condensation). We repeated our reprogramming assays with inducible four-factor OKSM reprogrammable
344 mouse embryonic fibroblasts and treated cells with a histone acetyl-transferase inhibitor during the 12 day
345 reprogramming period. Inhibition of HAT activity led to almost complete inhibition of Oct4-GFP positive
346 colonies and addition of exogenous putrescine rescued the inhibitory effects of HAT inhibition to levels
347 equivalent to the vehicle-treated condition (Fig. 6E and sFig. 7A). Exogenous putrescine was also able to rescue
348 the inhibitory effect of HAT inhibition on differentiation of 10T1/2 cells to adipocytes, which unlike chondrocyte
349 differentiation, requires polyamines (sFig. 7B). These experiments support a model in which polyamine
350 perturbations drive changes in cell fate as a result of their ability to increase histone tail dynamics (Fig. 6F).
351
352 **Discussion**
353 Here we propose that cells modulate their ability to rearrange chromatin structure by changing polyamine
354 levels. Mechanistically, our data are consistent with a model whereby interactions between histone tails and

355 nucleosomal DNA limit the activity of chromatin-modifying enzymes. Polyamines, by neutralizing negative
356 charges on the DNA backbone, weaken this interaction, allowing increased tail accessibility that facilitates
357 chromatin-modifying enzyme activity (Fig. 6F). This model is supported *in vivo* by the enrichment of
358 polyamines in the nucleus and the fact that DFMO impairs the activity of both chromatin writers and erasers
359 (Fig. 4B and sFig. 5I). Moreover, histone tail dynamics are enhanced by polyamines *in vitro* in 3 orthogonal
360 assays: chromatin-modifying assays, trypsin digestion of histone tails and NMR CSP and relaxation
361 experiments. The model is additionally supported by a) the lack of effects of polyamines when chromatin-
362 modifying enzymes act on histone protein alone (Fig. 4E and sFig. 5K,M); b) that a histone modification that is
363 not on the tail, but on the nucleosome core (H3K79 di-methylation), is unaffected by polyamine levels both *in*
364 *vivo* and *in vitro* (Fig. S5O-P); and c) that incubation of nucleosomes with polyamines does not denature the
365 nucleosome (Fig. S5N). This histone tail dynamics model provides an explanation for the longstanding
366 observation that spermidine and spermine enhance the efficacy of chromatin-based assays[57] . Our work also
367 underscores the importance of considering these abundant charged metabolites when modeling the structures
368 of protein-protein and protein-nucleic acid interactions. Interestingly, the one chromatin-modifying enzyme
369 reaction that was unaffected by polyamines was histone deacetylation (Fig. 4H). Since acetylated histone tails
370 already show increased dynamics[41,51–53] , it is not surprising that deacetylation efficiency would not be further
371 improved by polyamines.
372
373 A question raised by our *in vitro* work is why different polyamine species have different effects on chromatin-
374 modifying enzyme activity and histone tail accessibility. Spermine showed the largest ability to increase tail
375 accessibility while spermidine had slightly less of an effect and putrescine showed no discernible alteration
376 compared to vehicle. However, the effects of spermine on chromatin-modifying enzyme activity were not
377 matched by concentrations of putrescine or spermidine that would provide equivalent charge concentrations.
378 We did find that spermidine readily improved trypsin tail digestion of the H3 N-terminus, while spermine
379 increased digestion of intermediate H3 fragments. This may be explained by the NMR relaxation analysis which

380 suggests that, while spermidine has a broader effect throughout the length of the tail, spermine is more
381 specific, effectively increasing dynamics in two areas centered around the most N-terminal residues and
382 residues 19 to 29 (Fig. 6). More in-depth studies and computational modeling will be required to determine how
383 these different species interact with nucleosomal DNA and differentially change the accessibility of histone
384 tails. However, we know of no situation *in vivo* where polyamine species are present in isolation. Since a mix of
385 polyamines leads to maximal effects on histone tail dynamics, we interpret that these changes also correspond
386 to the changes occurring in nuclear chromatin *in vivo*.
387
388 We show that putrescine can substitute for MYC in the setting of reprogramming to pluripotency. Our model
389 suggests that polyamines increase the efficiency of the chromatin remodeling reactions necessary for de-
390 differentiation. Whether this increased efficiency is genome-wide, mediated through transcription factor-
391 dependent recruitment of chromatin-modifying enzymes or through sub-nuclear compartment-driven
392 localization of these metabolites is the focus of ongoing work. Transformed cancer cells also take on a less
393 differentiated state and, in many cases, upregulate polyamine biosynthesis. Accordingly, we found that
394 depletion of polyamines led to decreased proliferation and upregulation of differentiation markers across a
395 panel of cancer cell lines. One intriguing hypothesis is that by upregulating polyamine biosynthesis,
396 transformed cells might acquire the capacity to alter chromatin structure, increasing lineage plasticity and
397 allowing them to better adapt to diverse stressors and environments.
398
399 Ascribing the cell fate phenotypes seen when polyamine levels are perturbed *in vivo* to their effects on
400 chromatin structure is made difficult by their abundance and diverse functions. Two experiments support the
401 idea that the cell fate changes seen by perturbing polyamines result from their effects on chromatin. Firstly,
402 one role of polyamines is that spermidine acts as a substrate for the post-translational modification of eIF5A on
403 lysine 50[14,58]. This modification, hypusination, enables translation elongation and termination of mRNAs
404 encoding poly-proline tracts and other tri-peptide motifs[26,27,59]. Previous studies have suggested that polyamine

levels impact differentiation through their regulation of hypusination[60]. However, that inhibition of hypusination leads to impaired differentiation of the lines studied in this work, while DFMO and ODC1 loss promote a differentiation-like phenotype, argue that inhibition of hypusination is not mediating the cell state changes seen when polyamines are depleted. Second, we show that exogenous putrescine can rescue the loss of reprogramming or adipocyte differentiation caused by histone-acetyl-transferase inhibition. While it is formally possible that this rescue is mediated by hypusination or other functions of polyamines, histone acetylation increases tail accessibility and thus we interpret that exogenous putrescine is reinstating this effect when acetylation is absent. Thus, we conclude that fluctuations in polyamine levels enable cells to restrict or alter cell states by regulating the accessibility of histone tails.

415 **Methods and Materials**

416 *Cell culture and drug treatments*

417 10T1/2 and C2C12 cells were cultured in DMEM with 10% FBS and 1% pen-strep. CRISPR knockout lines were
418 generated by cloning pLentiCRISPRv2 (Addgene 98290) plasmids with sgRNA sequences targeting ODC1 or the
419 Rosa safe harbor locus. 293T cells were transfected with PEI with the targeting plasmid and pMD2 (Addgene
420 12259) and psPAX2 (Addgene 12260) vectors to generate viral supernatants, which was harvested 24-48 hours
421 after transfection and applied to target cells derived from single cell clones in the presence of 8 µg/mL
422 polybrene. Knockout lines were generated from single cells clones after puromycin selection and passaged in
423 media supplemented with 0.5 mM putrescine to rescue growth, then moved to media without putrescine for
424 the duration of experiments. SK-N-BE(2) cells were cultured in DMEM F-12 media with 10% FBS and 1% pen-
425 strep, COLO858 cells were cultured in RPMI with 5% FBS, 1% pen-strep and 1% sodium pyruvate, and K562
426 cells were cultured in RPMI with 20% FBS and 1% pen-strep. Cells were treated with 1 mM DFMO, 1 mM
427 putrescine, 0.5 µM GC7, 1 µM UNC0368, 0.5 mM octyl-R-2HG, 25 µM JG2016, 0.5 µM Vorinostat, or 1 µM
428 EPZ5676. For differentiation experiments, confluent 10T cells were exposed to chondrocyte differentiation
429 media (DMEM containing 1% FBS, 1% pen-strep, 3e-8M sodium selenite, 10 µg/mL insulin, 1e-8M
430 dexamethasone, 10 µg/mL transferrin, and 100ng/mL BMP-2). Confluent C2C12 cells were exposed to myotube
431 differentiation media (DMEM containing 1% pen-strep and 2% horse serum). K562 cells were exposed to
432 erythrocyte differentiation media (RPMI containing 40µM hemin) Differentiation media was refreshed every
433 two to three days. For growth curves, 15,000 cells were plated in triplicate, and counted using a Beckman-
434 Coulter Multisizer 3. For viability analysis, cells were stained with Trypan Blue, and counted using a Countess 3
435 Automated Cell Counter (ThermoFisher). All lines were determined to be mycoplasma free using MycoAlert
436 Detection Kit (Lonza).

437

438 *Western Blots*

439 Protein lysates were harvested from cells on ice with 1X RIPA buffer supplemented with protease and
440 phosphatase inhibitors (Thermo Fisher # 1860932 and Thermo Fisher # 78428, respectively). For experiments in
441 which histone marks were assayed, lysates were harvested in 1X RIPA buffer with 10% SDS and sonicated with
442 a Bioruptor Plus (Diagenode). Protein was separated on NuPAGE 4-12% Bis-Tris gels (Invitrogen NP0336),
443 blocked in 5% non-fat milk, and incubated with primary antibodies. After washing and secondary antibody
444 incubation, blots were incubated in 1-shot ECL solution (Kindle Biosciences LLC) and imaged with a ChemiDoc
445 MP Imaging System (BioRad).

446

447 *EdU and OPP incorporation and flow cytometry*

448 Cells were treated for 25 minutes with 20 µM EdU or 20 µM OPP (Thermo Fisher C10456). Following this pulse,
449 EdU-labeled cells were harvested, washed three times with 1% BSA in PBS, and fixed with 4%
450 paraformaldehyde (PFA). After fixation, cells were permeabilized with 0.5% Triton X-100 in PBS, washed three
451 times, and incubated in click chemistry reaction mix (2 mM $CuSO_4$, 8 µM sulfo-azide dye, 20 mg/mL ascorbic
452 acid in PBS) for 30 minutes in the dark. Cells were then washed, incubated in Hoechst (4 µg/mL), and EdU
453 incorporation was assayed by flow cytometry (NovoCyte Quanteon).

454

455 OPP-pulsed cells were fixed in ice-cold methanol for 10 minutes at –20°C, washed in 1% BSA in PBS, and
456 permeabilized with 0.5% Triton X-100. Cells were stained with homemade click chemistry reaction mix for
457 thirty minutes, washed, and analyzed by flow cytometry (NovoCyte Quanteon).

458

459 *Gas chromatography mass spectrometry*

460 GC-MS data collected over a time course of zebrafish embryonic development was analyzed from Dhillon et al.,
461 2019[61].

462

463 For extraction, chromatography and mass spectrometry analysis, cells were harvested in 80% Methanol,
464 Optima LC/MS Grade, (Fisher Chemical) overnight at -80˚C and dried using a Speed Vac Vacuum Concentrator
465 (Savant) attached to a Universal Vacuum System (Savant). Samples were resuspended in an extraction buffer
466 (10% NaCl solution made pH 1 with 0.5 M HCl) and polyamines were extracted with diethyl ether. Polyamines
467 were derivatized by extracting two times with 15% ethyl chloroformate in diethyl ether and dried under a
468 nitrogen stream. After another round of derivatization with trifluoroacetic anhydride in ethyl acetate, samples
469 were dried under a nitrogen stream and resuspended in ethyl acetate. Polyamines were measured with the
470 Agilent 8890/5977C gas chromatography/mass selective detector (GC/MSD). For LCMS, dried metabolites were
471 resuspended in water with N-octyl-amine internal standard (0.025 µM) with 5 µL of 1M sodium bicarbonate (pH
472 9). Samples were derivatized with isobutyl chloroformate for 15 minutes at 37°C followed by diethyl ether
473 extraction and drying of the organic phase under nitrogen stream. Samples were resuspended in 1:1
474 acetonitrile:water and 1 µL was analyzed on a Vanquish Duo UHPLC coupled to an Orbitrap ID-X Tribrid mass
475 spectrometer (Thermo Fisher Scientific) via a heated electrospray ionization (HESI) source. Samples were
476 injected in a randomized order to minimize batch effect. Samples were resolved by Reverse Phase
477 Chromatography using an Acquity UPLC BEH C18 column (2.1 x 150 mm, 1.7 µM, Waters) maintained at 40 °C.
478 The mobile phases consisted of (A) 0.1% formic acid in water, and (B) 0.1% formic acid in acetonitrile. Mobile
479 phases were delivered as follow: from 0 to 3 minutes, 0% B (300 µL/min); from 3 to 16 minutes, 0% to 40% B
480 linear gradient (300 µL/min); from 16 to 19 minutes, 40% to 100% B linear gradient (300 µL/min); from 19 to 21
481 minutes, 100% B (300 µL/min); from 21 to 21.9 minutes, 100% to 0% B linear gradient (300 µL/min); from 21.9
482 to 22 minutes, 0% B (300 µL/min); from 22 to 23.6 minutes, 0% B (500 µL/min); from 23.6 to 24 minutes, 0% B
483 (300 µL/min). Eluates were ionized using a HESI source alternating between +3.5 kV to -2.5 kV potential
484 (capillary temperature= 250 °C, sheath gas flow rate= 35 a.u., auxiliary gas flow= 5 a.u., and sweep gas flow= 1
485 a.u.). Ions were measured over a m/z range of 100-1000 using the orbitrap detector at 60,000 resolution (profile
486 mode). The automatic gain control (AGC) target was set to standard with automatic maximum injection time
487 control. Spectral data were processed using FreeStyle software (Thermo Fisher Scientific) and Skyline v.24.1

488 (McCoss Lab, University of Washington; MacLean B. et al., 2010, PMID: 20147306). For LC-MS experiments,
489 quantitative analysis was performed on raw peak areas of standard-validated metabolites meeting the
490 following criteria: coefficient of variation (CV) less than 30% in pooled quality control samples, signal-to-noise
491 ratio (S/N) greater than 3, mass accuracy within 5 ppm, and absence of detectable signal in blank controls.
492
493 *RNAseq, scRNAseq analysis, ATACseq, and MNase digestion*
494 RNAseq data was analyzed from the following repositories: GSE129957, GSE99399, GSE106292, GSE122380,
495 GSE42519, and the LIBD Stem Cell Browser[62].
496
497 RNA was harvested from cells (RNeasy Mini Kit, Qiagen 74104), and quality control was performed by
498 Tapestation analysis (Agilent). Libraries were prepared with the TruSeq Stranded mRNA Library Prep Kit
499 (Illumina) and sequenced on an AVITI system (Element Biosciences) using paired-end sequencing. bases2fastq
500 was used to demultiplex the data, and reads were mapped to the mouse genome (GRCm10) using kallisto.
501 Count matrices were analyzed in R using DESeq2.
502
503 For single cell analysis of erythroid differentiation, the count matrix was downloaded from GSE196347
504 containing transcriptomes from sorted CD71+ murine bone marrow sequenced on an Illumina NovaSeq and
505 quantified using the Cell Ranger workflow. Dimensionality reduction and visualization were conducted by first
506 learning the latent representation of the data using scVI[63], a tool that models gene expression using a deep
507 neural network. The model was run with 1 hidden layer, a latent space of dimension 10, and a dropout rate of
508 0.1. The scVI latent variables were used as input to the Scanpy UMAP function (sc.tl.umap) to produce a low-
509 dimensional visualization of the data. Leiden clustering (sc.tl.leiden) was performed using a resolution of 0.5 to
510 capture broad cell types, generating nine clusters. Each cluster was interrogated for expression of Hba-a1,
511 Gypa, Slc4a1, and Tfrc. Two clusters were removed due to high mitochondrial gene expression or lack of Hba-a1
512 expression. Modeling of the data was repeated after cluster removal.

513

514 To reconstruct the progression of cells through erythropoiesis, PAGA[64] was used to infer a trajectory
515 (sc.pl.paga). A 'root cell' was determined based on the expression patterns of Tfrc, Klf1, Gata1, Xpo7, Tmcc2,
516 and Bpgm, indicating the cluster at the start site of the trajectory[65–69]. The diffusion pseudotime was calculated
517 using sc.tl.diffmap and sc.tl.dpt. Gene expression plotted against pseudotime was smoothed using the
518 LOWESS (Locally Weighted Scatterplot Smoothing) tool in the statsmodels module. Confidence intervals were
519 calculated by determining the standard deviation of 50 curves generated from a sampling of 500 data points
520 (with replacement). The track plot was generated using sc.pl.tracksplot, with the groups (Ery1, Ery2, Ery3,
521 Ery4, and Ery5) reflecting the Leiden clusters in order of pseudotime. Expression of essential erythropoietic
522 genes and genes specific for hematopoietic progenitors, myeloid cells, lymphoid cells, and megakaryocytes
523 were used to validate the generated pseudotime trajectory.

524

525 ATACseq library preparation was carried out as previously described[70] and included a spike-in of 0.1 ng E. coli
526 DNA per sample (EpiCypher # 18-1401). Libraries were amplified with NEBNext Multiplex Oligos (Illumina), and
527 quality control was performed with Tapestation (Agilent) and KAPA library quantification (Roche). Libraries
528 were sequenced on an AVITI system (Element Biosciences) using paired-end sequencing, and quality control
529 was performed using FASTQC. Reads were trimmed using Trimgalore, and aligned to GRCm10 and the NCBI E.
530 coli K12 genome using Bowtie2. Sorting and duplicate removal was performed using Samtools and Picard, and
531 peaks were called with MACS2. Depth normalization to E. coli internal standards, and differential peak analysis,
532 was performed using DiffBind. Peaks were annotated with ChipSeeker and CHIPpeakAnno, and reads were
533 indexed for visualization with Samtools.

534

535 For MNase digestion experiments, nuclei from 147,000 cells per sample were incubated in 1 U MNase
536 (ThermoFisher, EN0181) per million cells for 15 minutes at 37°C. DNA was extracted and quantified on a Qubit
537 (ThermoFisher). 3 ng DNA per sample was analyzed with a high sensitivity Tapestation (Agilent).

538

539 *Polyamine probe and microscopy*

540 Putrescine, spermidine, and spermine azide probes were synthesized as previously described[71], without the
541 addition of the BoDiPY moiety. Probes were resuspended in media at 10 µM and applied to live cells for two
542 hours. Cells were then washed, fixed with 4% paraformaldehyde, permeabilized with 0.1% Triton-X in PBS, and
543 incubated in homemade click chemistry reaction cocktail (2 mM $CuSO_4$, 50mM THPTA, 8 µM alkyne-
544 conjugated fluorophore, 20 mg/mL ascorbic acid) for 30 minutes. Following click chemistry reactions, cells were
545 stained with Hoechst or DAPI, and imaged on a Zeiss LSM 780 confocal microscope.

546

547 For zebrafish probe experiments, AB wildtype embryos were manually dechorionated at the four-cell stage and
548 moved into water containing 10 µM polyamine probe for 2 hours. Embryos were then fixed for 20 minutes with
549 4% PFA, permeabilized with 0.1% Triton X-100 in PBS, incubated in homemade click chemistry reaction
550 cocktail with an alkyne-conjugated fluorophore for 30 minutes, and then DNA was stained with Hoechst. Yolk
551 was removed by manual dissection and embryos were mounted for imaging on a Zeiss LSM 780 confocal
552 microscope. The Institutional Animal Care and Use Committees of Columbia University approved all zebrafish
553 experiments.

554

555 *In vitro enzymatic assays*

556 All *in vitro* reactions were carried out with 1 µg nucleosome or histone protein substrate and 2.8 µg enzyme in
557 40 µL reaction buffer. Reactions were halted by addition of NuPAGE sample buffer, boiled at 95°C for 5
558 minutes, and then split in two and run on separate NuPAGE 4-12% Bis-Tris gels for analysis by western blot. *In*
559 *vitro* demethylase reaction buffer contained 50 mM Tris-HCl pH 8.0, 5% glycerol, 2 mM ascorbate, 1 mM alpha-
560 ketoglutarate, 100 µM $FeSO_4$, 50 mM KCl, and protease inhibitor. *In vitro* demethylase reactions were carried
561 out at 37°C for two hours. *In vitro* methyl-transferase reaction buffer contained 50 mM Tris-HCl pH 8.0, 5 mM
562 $MgCl_2$, 10 µM SAM, 4 mM DTT, and protease inhibitor. *In vitro* methyl-transferase reactions were carried out at

563 37°C for one hour. *In vitro* deacetylase reaction buffer contained 25 mM Tris-HCl pH 8.0, 50 mM NaCl, 1 mM
564 DTT, 5 mM NAD+ and protease inhibitor. *In vitro* deacetylase reactions were carried out at 37°C for 15 minutes.
565 *In vitro* acetylase reaction buffer contained 50 mM Tris-HCl pH 8.0, 5% glycerol, 1 mM DTT, 50 mM NaCl, 100
566 µM acetyl CoA, and protease inhibitor. *In vitro* acetylase reactions were carried out at 37°C for one hour.
567
568 Trypsin tail digestion reactions were carried out with 2 µg nucleosome or histone protein substrate and 10 ng
569 trypsin in 10 µL reaction buffer. Reactions were halted by addition of Tricine sample buffer, boiled at 95°C for
570 10 minutes, and run on a Novex Tricine 16% mini protein gel. Gels were stained with Imperial protein stain.
571 Trypsin digestion buffer contained 20mM MOPS, 1mM EDTA, and 1mM DTT.
572
573 To assess nucleosome integrity after polyamine incubation, mononucleosomes were incubated for one hour at
574 37°C in the presence of 100 µM putrescine, spermidine, or spermine. A digested control sample was processed
575 with the Zymo Research Clean and Concentrate Kit. Samples were run on a 1.5% agarose gel, DNA was stained
576 with ethidium bromide, and the gel was imaged on a ChemiDoc MP Imaging System (BioRad).
577
578 *Histone purification and nucleosome reconstitution for NMR*
579 Histones and DNA were purified and reconstituted as outlined in Dyer et al[72]. Unmodified human histones
580 (H2A.1 Uniprot accession P0C0S8, H2B.1C Uniprot accession P62807, H4 Uniprot accession P62805, and H3.2
581 Uniprot accession Q71DI3 with C110A and G102A) were expressed in Rosetta 2 (DE3) pLysS (Novagen) or BL21
582 (DE3) (New England Biolabs) chemically competent E. coli. Unlabeled growths were carried out in LB and
583 induced at OD600~0.4 with 0.2 mM (for H4) or 0.4mM (for H2A, H2B, and H3) IPTG for 3-4 hours. ^{15}N-
584 isotopically enriched H3 was grown in M9 minimal media supplemented with vitamin (Centrum) and 1 g L-
585 $^{15}NH_4Cl$. Histones were extracted from inclusion bodies and purified via ion exchange chromatography.
586 Histones were validated using ESI mass spectrometry (Fig. S6C). For DNA purification, a plasmid containing 37
587 repeats of the 147 bp Widom 601 sequence (ATCGAGAATC CCGGTGCCGA GGCCGCTCAA TTGGTCGTAG

588 ACAGCTCTAG CACCGCTTAA ACGCACGTAC GCGCTGTCCC CCGCGTTTTA ACCGCCAAGG GGATTACTCC
589 CTAGTCTCCA GGCACGTGTC AGATATATAC ATCCGAT) was amplified in E. coli and purified via alkaline lysis
590 methods. The 601 repeats were released by cleavage with EcoRV and purified from parent plasmid by
591 polyethylene glycol precipitation. Nucleosome reconstitutions were prepared by refolding tetramer (with
592 equimolar ratios of H3 and H4) and dimer (with equimolar ratios of H2A and H2B) separately. Tetramer, dimer,
593 and 601 DNA were then mixed together at a 1:2.2:1 molar ratio. Both mixtures were then desalted using a linear
594 gradient from 2 M to 150 mM NaCl over 36-48 hours, followed by dialysis against 0.5xTE. Samples were then
595 purified with a 10-40% sucrose gradient, which separates residual free 601 DNA and any subnucleosomal
596 particles (i.e. tetrasome and hexasome). Native- and SDS-PAGE were used to assess the formation of
597 nucleosomes along with histone composition (see Fig. S6A). Bands were visualized with ethidium bromide or
598 Coomassie for native and denaturing gels, respectively. Nucleosomes were then dialyzed into 20 mM MOPS pH
599 7, 100 mM NaCl, 1 mM DTT, 1 mM EDTA for the purposes of NMR titrations. Concentrations were determined
600 via UV-vis spectroscopy using the absorbance from the 601 DNA (calculated ε260 = 2,312,300.9 M-1cm-1).
601 Samples were diluted into 2 M NaCl prior to concentration measurements in order to promote nucleosome
602 disassembly for more accurate concentration determination.
603
604 *NMR Titration*
605 ^{1}H,^{15}N heteronuclear single quantum coherence ($^{1}H^{15}N$-HSQC) spectra of ^{15}N-labelled ^{15}N-H3-NCP (128 μM) in
606 20 mM MOPS pH 7, 100 mM NaCl, 1 mM DTT, 1 mM EDTA, and 10% D_2O were measured at varying spermidine
607 trichloride concentrations. All the HSQC spectra were measured at 37°C on a Bruker Avance Neo 600 MHz
608 spectrometer equipped with a room temperature probe. The NMR spectra were processed in NMRPipe and
609 analyzed using Sparky[73]. The normalized chemical shift difference (Δδ) was calculated using the following
610 equation:

$$\Delta\delta = \sqrt{(\Delta\delta_H)^2 + (0.154\Delta\delta_N)^2}$$

611 Where ΔδH and ΔδN are the observed changes in the ^{1}H and ^{15}N chemical shifts, respectively, upon addition of
612 spermidine or spermine trichloride.
613
614 *NMR ^{15}N Relaxation analysis*
615 The backbone ^{15}N longitudinal relaxation rates (R1), and transverse relaxation rate (R2) of ^{15}N-H3 -NCP, in both
616 the apo and spermidine trichloride or spermine bound-form were measured on a Bruker NEO 600 MHz
617 spectrometer at 37°, using gradient enhanced phase-sensitive HSQC pulse sequences (hsqct1etf3gpsitc3d and
618 hsqct2etf3gpsitc3d). The ^{15}N-H3-NCP (128 µM) sample and the ^{15}N-H3-NCP sample with 512 µM spermidine or
619 spermine were prepared in a buffer containing 20 mM MOPS (pH 7), 100 mM NaCl, 1 mM DTT, 1 mM EDTA, and
620 10% D_2O. The ^{15}N-R1 experiments were conducted with relaxation delays of 25, 200, 400, 800, 1250, and 1750
621 ms. In the ^{15}N-R2 experiments the relaxation delays were set to 15.68, 31.36, 47.04, 62.72, 94.08, and 109.76 ms.
622 The ^{15}N-R1, and ^{15}N-R2, experiments were processed in NMRPipe. The R1 and R2 relaxation rates were
623 determined by least-square fitting of the amide peak intensities to a single exponential decay function.
624 Subsequently, the rotational correlation time, τ_c was calculated from R1 and R2 using the following equation:

$$\tau_c = \frac{1}{4\pi\vartheta_N}\sqrt{6\frac{R_2}{R_1} - 7}$$

625 Where ϑ_N is the resonance frequency of ^{15}N.
626 The error in R1 and R2 were propagated to R2/R1, and then to τ_c using standard error propagation.
627
628 *Reprogramming*
629 Mouse embryonic fibroblasts (MEFs) expressing either doxycycline-inducible OSK or OSKM were
630 reprogrammed as previously described[74]. Briefly, cells were seeded on a layer of feeder MEFs, then transferred
631 into induction media (DMEM with 15% FBS, 1% non-essential amino acids, 1% GlutaMAX, beta-mercapto-
632 ethanol and 1000 U/mL LIF) containing 1 mg/mL doxycycline and either 1 mM DFMO,1 mM putrescine, or 1 µM
633 A485 (HATi). Media was refreshed every two days for twelve days, and then cells were moved into induction

634 media without doxycycline for four days. Doxycycline-independent GFP-positive colonies were counted
635 manually, and then live cells were dissociated for analysis by flow cytometry on a NovoCyte Quanteon.
636

637 **Acknowledgements**

638 We thank C. Chio (Columbia University) and C. Lu (Columbia University) for antibody reagents and E. Mikhail
639 Yohannan Cheria (Columbia University) for assistance with GCMS. Three and four factor reprogrammable
640 fibroblasts were a gift from M. Stadtfeld (Weill Cornell Medical College). Flow cytometry and confocal
641 microscopy were performed in the Columbia Stem Cell Initiative Flow Cytometry Institutional Core facility and
642 the Columbia Medicine Microscopy Core. The histone acetyl-transferase inhibitor JG2016 was a gift from J.
643 Gruber (UT Southwestern Medical Center). We thank C. Chio, C. Lu, S. Sternberg and L. Johnston for critical
644 reading of the manuscript.
645

646 **Funding**

647 J.M.S. was supported by W81XWH-21-1-0292 US Army Medical Research and Development Command
648 (USAMRDC), Department of Defense and National Institutes of Health (NIH; 1R35GM154927). M.E.B. was
649 supported by a Hope Funds for Cancer Research Postdoctoral Fellowship. Work in the Smeeton lab was
650 supported by the National Institute of Dental & Craniofacial Research (NIH; DP2DE032725). Work in the
651 Musselman laboratory is funded by the National Institutes of Health (NIH; R35GM128705). NMR spectrometers
652 are funded by the National Institutes of Health (NIH; P30 CA046934 and S10 OD014010-01).
653

654 **Author Contributions**

655 Conceptualization: MEB, JMS
656 Methodology: MEB, MRR, GF, AJS, SO, AG, RS, JC, SV, MHK, JS, SA, HAF, CM
657 Investigation: MEB, MRR, GF, AJS, SO, AG, RS, JC, MHK, SA, HAF, VSS, EMS
658 Data Curation: MEB, MRR, GF, AJS, SV, MHK, JS, SA, VSS, EMS, CM, JMS

Formal Analysis: MEB, MRR, GF, AJS, SV, JS, ADV, CM, JMS

Visualization: MEB, CM, JMS

Funding Acquisition: MEB, CM, JMS

Project Administration: JMS

Supervision: JMS

Writing – original draft: MEB, JMS

Writing – review & editing: MEB, JMS

Competing Interests

MEB and JMS are authors of a patent submitted by Columbia University related to this work. All other authors declare that they have no competing interests.

Data and Materials Availability

All data and materials are available upon request. Sequencing data are deposited with the NCBI GEO (accession pending).

675 **References**

676

677 1. Holbert, C. E., Cullen, M. T., Casero, R. A. & Stewart, T. M. Polyamines in cancer: integrating organismal
678 metabolism and antitumour immunity. *Nat Rev Cancer* **22**, 467–480 (2022).
679 2. Alhonen-Hongisto, L., Seppänen, P. & Jänne, J. Intracellular putrescine and spermidine deprivation induces
680 increased uptake of the natural polyamines and methylglyoxal bis(guanylhydrazone). *Biochem. J.* **192**, 941–945
681 (1980).
682 3. Chen, W. W., Freinkman, E., Wang, T., Birsoy, K. & Sabatini, D. M. Absolute Quantification of Matrix
683 Metabolites Reveals the Dynamics of Mitochondrial Metabolism. *Cell* **166**, 1324 1337.e11 (2016).
684 4. Ray, R. M., Zimmerman, B. J., McCormack, S. A., Patel, T. B. & Johnson, L. R. Polyamine depletion arrests cell
685 cycle and induces inhibitors p21Waf1/Cip1, p27Kip1, and p53 in IEC-6 cells. *Am. J. Physiol.-Cell Physiol.* **276**,
686 C684–C691 (1999).
687 5. Cheetham, B. F. An Inhibitor of Polyamine Synthesis Arrests Cells at an Earlier Stage of G1 than Does Calcium
688 Deprivation. *Mol. Cell. Biol.* **3**, 480–483 (1983).
689 6. Heby, O., Andersson, G. & Gray, J. W. Interference with S and G2 phase progression by polyamine synthesis
690 inhibitors. *Exp. Cell Res.* **111**, 461–464 (1978).
691 7. Jetten, A. M. & Shirley, J. E. Inhibition of ornithine decarboxylase by retinoic acid and difluoromethylornithine
692 in relation to their effects on differentiation and proliferation. *Exp Cell Res* **156**, 221–230 (1985).
693 8. Oredsson, S. M., Billgren, M. & Heby, O. Induction of F9 embryonal carcinoma cell differentiation by
694 inhibition of polyamine synthesis. *Eur J Cell Biol* **38**, 335–43 (1985).
695 9. Choudhary, S. K., Sharma, D. & Dixit, A. D,L-alpha-difluoromethylornithine, an irreversible inhibitor of
696 ornithine decarboxylase, induces differentiation in MEL cells. *Cell Biol. Int.* **23**, 489–495 (1999).
697 10. Bello-Fernandez, C., Packham, G. & Cleveland, J. L. The ornithine decarboxylase gene is a transcriptional
698 target of c-Myc. *Proc National Acad Sci* **90**, 7804–7808 (1993).

699 11. Nilsson, J. A. *et al.* Targeting ornithine decarboxylase in Myc-induced lymphomagenesis prevents tumor
700 formation. *Cancer Cell* **7,** 433–444 (2005).
701 12. Hogarty, M. D. *et al.* ODC1 Is a Critical Determinant of MYCN Oncogenesis and a Therapeutic Target in
702 Neuroblastoma. *Cancer Res* **68,** 9735–9745 (2008).
703 13. Park, M. H., Cooper, H. L. & Folk, J. E. Identification of hypusine, an unusual amino acid, in a protein from
704 human lymphocytes and of spermidine as its biosynthetic precursor. *Proc. Natl. Acad. Sci.* **78,** 2869–2873 (1981).
705 14. Cooper, H. L., Park, M. H., Folk, J. E., Safer, B. & Braverman, R. Identification of the hypusine-containing
706 protein hy+ as translation initiation factor eIF-4D. *Proc National Acad Sci* **80,** 1854–1857 (1983).
707 15. Lopatin, A. N., Makhina, E. N. & Nichols, C. G. Potassium channel block by cytoplasmic polyamines as the
708 mechanism of intrinsic rectification. *Nature* **372,** 366–369 (1994).
709 16. Benning, N. A. *et al.* Dimensional Reduction for Single-Molecule Imaging of DNA and Nucleosome
710 Condensation by Polyamines, HP1α and Ki-67. *J. Phys. Chem. B* **127,** 1922–1931 (2023).
711 17. Park, S. *et al.* Native nucleosomes intrinsically encode genome organization principles. *Nature* 1–10 (2025)
712 doi:10.1038/s41586-025-08971-7.
713 18. Feuerstein, B. G., Pattabiraman, N. & Marton, L. J. Molecular mechanics of the interactions of spermine with
714 DNA: DNA bending as a result of ligand binding. *Nucleic Acids Res* **18,** 1271–1282 (1990).
715 19. Kanemura, A. *et al.* Opposite effect of polyamines on *In vitro* gene expression: Enhancement at low
716 concentrations but inhibition at high concentrations. *Plos One* **13,** e0193595 (2018).
717 20. Kleppe, K. *et al.* Effect of polyamines on enzymes involved in DNA repair. *Med Biol* **59,** 374–80 (1981).
718 21. Snyder, R. D. Polyamine depletion is associated with altered chromatin structure in HeLa cells. *Biochem J*
719 **260,** 697–704 (1989).
720 22. Chen, G. G., Turecki, G. & Mamer, O. A. A quantitative GC-MS method for three major polyamines in
721 postmortem brain cortex. *J. Mass Spectrom.* **44,** 1203–1210 (2009).
722 23. Taylor, S. M. & Jones, P. A. Multiple new phenotypes induced in 10T12 and 3T3 cells treated with 5-
723 azacytidine. *Cell* **17,** 771–779 (1979).

724 24. Choi, S.-H., Kim, S.-W., Choi, D.-H., Min, B.-H. & Chun, B.-G. Polyamine-depletion induces p27Kip1 and
725 enhances dexamethasone-induced G1 arrest and apoptosis in human T lymphoblastic leukemia cells. *Leuk. Res.*
726 **24,** 119–127 (2000).
727 25. Pelechano, V. & Alepuz, P. eIF5A facilitates translation termination globally and promotes the elongation of
728 many non polyproline-specific tripeptide sequences. *Nucleic Acids Res.* **45,** 7326–7338 (2017).
729 26. Schuller, A. P., Wu, C. C.-C., Dever, T. E., Buskirk, A. R. & Green, R. eIF5A Functions Globally in Translation
730 Elongation and Termination. *Mol. Cell* **66,** 194-205.e5 (2017).
731 27. Gutierrez, E. *et al.* eIF5A Promotes Translation of Polyproline Motifs. *Mol. Cell* **51,** 35–45 (2013).
732 28. Park, M. H. & Wolff, E. C. Hypusine, a polyamine-derived amino acid critical for eukaryotic translation. *J.*
733 *Biol. Chem.* **293,** 18710–18718 (2018).
734 29. Pakos-Zebrucka, K. *et al.* The integrated stress response. *EMBO Rep.* **17,** 1374–1395 (2016).
735 30. Trefely, S. *et al.* Quantitative subcellular acyl-CoA analysis reveals distinct nuclear metabolism and
736 isoleucine-dependent histone propionylation. *Mol Cell* **82,** 447-462.e6 (2022).
737 31. Kafkia, E. *et al.* Operation of a TCA cycle subnetwork in the mammalian nucleus. *Sci Adv* **8,** eabq5206
738 (2022).
739 32. Alexandrov, T. Spatial metabolomics: from a niche field towards a driver of innovation. *Nat. Metab.* **5,** 1443–
740 1445 (2023).
741 33. Gamble, L. D. *et al.* Inhibition of polyamine synthesis and uptake reduces tumor progression and prolongs
742 survival in mouse models of neuroblastoma. *Sci Transl Med* **11,** (2019).
743 34. Gao, W. *et al.* Polyamine depletion limits progression of acute leukaemia. *Int. J. Cancer* (2025)
744 doi:10.1002/ijc.35362.
745 35. Corral, M. & Wallace, H. M. Upregulation of Polyamine Transport in Human Colorectal Cancer Cells.
746 *Biomolecules* **10,** 499 (2020).
747 36. Yoo, J., Kim, H., Aksimentiev, A. & Ha, T. Direct evidence for sequence-dependent attraction between
748 double-stranded DNA controlled by methylation. *Nat. Commun.* **7,** 11045 (2016).

749 37. Pan, W., Zhou, J., Yin, Y., Wen, H. & Liang, D. Local de-condensation of double-stranded DNA in oppositely
750 charged polyelectrolyte as induced by spermidine. *Soft Matter* **11**, 4705–4709 (2015).
751 38. Lu, C. *et al.* IDH mutation impairs histone demethylation and results in a block to cell differentiation. *Nature*
752 **483**, 474 478 (2012).
753 39. Karch, K. R. *et al.* Hydrogen-Deuterium Exchange Coupled to Top- and Middle-Down Mass Spectrometry
754 Reveals Histone Tail Dynamics before and after Nucleosome Assembly. *Structure* **26**, 1651-1663.e3 (2018).
755 40. Musselman, C. A. & Kutateladze, T. G. Visualizing Conformational Ensembles of the Nucleosome by NMR.
756 *ACS Chem. Biol.* **17**, 495–502 (2022).
757 41. Stützer, A. *et al.* Modulations of DNA Contacts by Linker Histones and Post-translational Modifications
758 Determine the Mobility and Modifiability of Nucleosomal H3 Tails. *Mol. Cell* **61**, 247–259 (2016).
759 42. Morrison, E. A., Bowerman, S., Sylvers, K. L., Wereszczynski, J. & Musselman, C. A. The conformation of the
760 histone H3 tail inhibits association of the BPTF PHD finger with the nucleosome. *eLife* **7**, e31481 (2018).
761 43. Imre, L. *et al.* Nucleosome destabilization by polyamines. *Arch. Biochem. Biophys.* **722**, 109184 (2022).
762 44. Daigle, S. R. *et al.* Selective Killing of Mixed Lineage Leukemia Cells by a Potent Small-Molecule DOT1L
763 Inhibitor. *Cancer Cell* **20**, 53–65 (2011).
764 45. Morrison, E. A., Baweja, L., Poirier, M. G., Wereszczynski, J. & Musselman, C. A. Nucleosome composition
765 regulates the histone H3 tail conformational ensemble and accessibility. *Nucleic Acids Res.* **49**, 4750–4767
766 (2021).
767 46. Ohtomo, H. *et al.* H2A Ubiquitination Alters H3-tail Dynamics on Linker-DNA to Enhance H3K27
768 Methylation. *J. Mol. Biol.* **435**, 167936 (2023).
769 47. Jennings, C. E., Zoss, C. J. & Morrison, E. A. Arginine anchor points govern H3 tail dynamics. *Front. Mol.*
770 *Biosci.* **10**, 1150400 (2023).
771 48. Takahashi, K. & Yamanaka, S. Induction of pluripotent stem cells from mouse embryonic and adult
772 fibroblast cultures by defined factors. *Cell* **126**, 663 676 (2006).

773 49. Stadtfeld, M., Maherali, N., Borkent, M. & Hochedlinger, K. A reprogrammable mouse strain from gene-
774 targeted embryonic stem cells. *Nat. Methods* **7**, 53–55 (2010).
775 50. Amlani, B. *et al.* Nascent Induced Pluripotent Stem Cells Efficiently Generate Entirely iPSC-Derived Mice
776 while Expressing Differentiation-Associated Genes. *Cell Rep.* **22**, 876–884 (2018).
777 51. Kim, T. H. *et al.* Correlating histone acetylation with nucleosome core particle dynamics and function. *Proc.*
778 *Natl. Acad. Sci.* **120**, e2301063120 (2023).
779 52. Marunde, M. R. *et al.* Nucleosome conformation dictates the histone code. *eLife* **13**, e78866 (2024).
780 53. Jain, K. *et al.* An acetylation-mediated chromatin switch governs H3K4 methylation read-write capability.
781 *eLife* **12**, e82596 (2023).
782 54. Huangfu, D. *et al.* Induction of pluripotent stem cells by defined factors is greatly improved by small-
783 molecule compounds. *Nat. Biotechnol.* **26**, 795–797 (2008).
784 55. Liang, G., Taranova, O., Xia, K. & Zhang, Y. Butyrate Promotes Induced Pluripotent Stem Cell Generation*.
785 *J. Biol. Chem.* **285**, 25516–25521 (2010).
786 56. Hirsch, C. L. *et al.* Myc and SAGA rewire an alternative splicing network during early somatic cell
787 reprogramming. *Genes Dev.* **29**, 803–816 (2015).
788 57. Hewish, D. R. & Burgoyne, L. A. Chromatin sub-structure. The digestion of chromatin DNA at regularly
789 spaced sites by a nuclear deoxyribonuclease. *Biochem. Biophys. Res. Commun.* **52**, 504–510 (1973).
790 58. Chattopadhyay, M. K., Park, M. H. & Tabor, H. Hypusine modification for growth is the major function of
791 spermidine in Saccharomyces cerevisiae polyamine auxotrophs grown in limiting spermidine. *Proc. Natl. Acad.*
792 *Sci.* **105**, 6554–6559 (2008).
793 59. Pelechano, V. & Alepuz, P. eIF5A facilitates translation termination globally and promotes the elongation of
794 many non polyproline-specific tripeptide sequences. *Nucleic Acids Res.* **45**, 7326–7338 (2017).
795 60. Puleston, D. J. *et al.* Polyamine metabolism is a central determinant of helper T cell lineage fidelity. *Cell*
796 (2021) doi:10.1016/j.cell.2021.06.007.

797 61. Dhillon, S. S. *et al.* Metabolic profiling of zebrafish embryo development from blastula period to early larval
798 stages. *PLoS ONE* **14,** e0213661 (2019).
799 62. Burke, E. E. *et al.* Dissecting transcriptomic signatures of neuronal differentiation and maturation using
800 iPSCs. *Nat. Commun.* **11,** 462 (2020).
801 63. Lopez, R., Regier, J., Cole, M. B., Jordan, M. I. & Yosef, N. Deep Generative Modeling for Single-cell
802 Transcriptomics. *Nat. methods* **15,** 1053–1058 (2018).
803 64. Wolf, F. A. *et al.* PAGA: graph abstraction reconciles clustering with trajectory inference through a topology
804 preserving map of single cells. *Genome Biol.* **20,** 59 (2019).
805 65. Mohandas, N. & Prenant, M. Three-dimensional Model of Bone Marrow. *Blood* **51,** 633–643 (1978).
806 66. Hattangadi, S. M. *et al.* Histones to the cytosol: exportin 7 is essential for normal terminal erythroid nuclear
807 maturation. *Blood* **124,** 1931–1940 (2014).
808 67. Nemkov, T. *et al.* Circulating primitive murine erythroblasts undergo complex proteomic and metabolomic
809 changes during terminal maturation. *Blood Adv.* **6,** 3072–3089 (2022).
810 68. Kumari, R. *et al.* Ablation of Tmcc2 Gene Impairs Erythropoiesis in Mice. *Int. J. Mol. Sci.* **23,** 5263 (2022).
811 69. Romano, L. *et al.* Erythroblastic islands foster granulopoiesis in parallel to terminal erythropoiesis. *Blood*
812 **140,** 1621–1634 (2022).
813 70. Corces, M. R. *et al.* An improved ATAC-seq protocol reduces background and enables interrogation of
814 frozen tissues. *Nat Methods* **14,** 959 962 (2017).
815 71. Vanhoutte, R., Kahler, J. P., Martin, S., Veen, S. van & Verhelst, S. H. L. Clickable Polyamine Derivatives as
816 Chemical Probes for the Polyamine Transport System. *Chembiochem* **19,** 907–911 (2018).
817 72. Dyer, P. N. *et al.* Reconstitution of Nucleosome Core Particles from Recombinant Histones and DNA.
818 *Methods Enzym.* **375,** 23–44 (2003).
819 73. Delaglio, F. *et al.* NMRPipe: A multidimensional spectral processing system based on UNIX pipes. *J. Biomol.*
820 *NMR* **6,** 277–293 (1995).

821 74. Vidal, S. E., Amlani, B., Chen, T., Tsirigos, A. & Stadtfeld, M. Combinatorial Modulation of Signaling
822 Pathways Reveals Cell-Type-Specific Requirements for Highly Efficient and Synchronous iPSC Reprogramming.
823 *Stem Cell Rep.* **3,** 574–584 (2014).
824
825

826 **Figure Legends**

827 **Figure 1**

828 A) Polyamines are synthesized by the irreversible decarboxylation of ornithine by ornithine decarboxylase
829 (ODC1), which is a direct transcriptional target of MYC, and inhibited by the drug
830 difluoromethylornithine (DFMO).

831 B) ODC1 expression from publicly-available RNAseq and scRNAseq (erythroid) data collected over time
832 courses of adipocyte, osteoblast, chondrocyte, neuronal, myotube, and erythroid differentiation. For
833 RNAseq samples, box plots display medians and quartiles of the data. P values correspond to T test
834 with Bonferroni correction. For scRNAseq data, plot shows mean +/- SEM and rho and p value
835 correspond to Spearman test.

836 C) Western blots showing induction of the erythroid marker Hemoglobin in K562 erythroblastic human
837 leukemia cells during ten days of differentiation, and of the myotube markers Myosin Heavy Chain and
838 MyoG in C2C12 cells after seven days of treatment with myotube differentiation media.

839 D) Quantification of relative polyamine levels over a time course of differentiation in K562 cells.
840 Abundance of each polyamine species was normalized to cell number. Spearman Correlation
841 coefficient and P value shown.

842 E) Quantification of relative polyamine levels over a time course of differentiation in C2C12 cells.
843 Abundance of each polyamine species was normalized to cell number. Spearman Correlation
844 coefficient and P value shown.

845

846 **Figure 2**

847 A) Control (sgRosa) and ODC1 knockout (sgODC1) cells were plated in media containing vehicle, 1 mM
848 DFMO, or 1 mM putrescine, and cells were counted one, three, and four days after seeding. Data
849 presented are mean +/- standard error of three biological replicates. P values calculated by T test with
850 Bonferroni correction.

851 B) Relative putrescine concentrations in control (sgRosa) and ODC1 knockout (sgODC1) cells following
852 three days of growth in putrescine-free media. Putrescine abundance was normalized to cell counts.
853 Error bars correspond to standard error. P values calculated by one-tailed t-test.
854 C) Morphology of control (sgRosa) and ODC1 knockout (sgODC1) cells following three days of indicated
855 treatments (1 mM DFMO, 1 mM putrescine). Scale bar is 275 µM.
856 D) Principal component analysis of RNAseq data from control (sgRosa) and ODC1 knockout (sgODC1)
857 cells. RNA was extracted from cells following three days of indicated treatments (1 mM DFMO, 1 mM
858 putrescine).
859 E) Gene set enrichment analysis comparing low-polyamine samples (control cells treated with DFMO, and
860 ODC1 knockout cells treated with vehicle or DFMO) to high-polyamine samples (control cells treated
861 with vehicle or putrescine, and ODC1 knockout cells treated with putrescine).
862 F) 10T1/2 cells were treated with either vehicle or DFMO-containing media and moved into indicated
863 treatments after three days. Cells were counted six days after plating (three days after media change).
864 Data presented are mean +/- standard error of three biological replicates. P values calculated by Dunn's
865 test.
866 G) Western blots showing markers of differentiation in progenitor and transformed cell lines. 10T1/2 cells
867 were treated with the indicated treatments (1 mM DFMO) in growth media for 24 hours and then
868 moved to differentiation media for 24 hours. C2C12 cells were treated with the indicated treatments (1
869 mM DFMO, 1 mM putrescine) in differentiation media. All transformed cell lines were treated with 1
870 mM DFMO in growth media.
871
872 **Figure 3**
873 A) Structure of the putrescine-azide probe.
874 B) Intracellular localization of the putrescine probe in 10T1/2 cells visualized by confocal microscopy
875 following three days of the indicated treatments (1 mM DFMO, 1 mM putrescine). Scale bars are 5 µM.

876 C) Intracellular localization of the spermidine probe in 10T1/2 cells visualized by confocal microscopy
877 following treatments as per B). Scale bars are 5 µM.
878 D) Intracellular localization of the spermine probe in 10T1/2 cells visualized by confocal microscopy
879 following treatments as per B). Scale bars are 5 µM.
880
881 **Figure 4**
882 A) Distribution of the fold change in peak accessibility in 10T1/2 cells treated with 1 mM DFMO or 1 mM
883 putrescine versus vehicle for three days as determined by ATACseq.
884 B) Western blots showing abundance of H3K27ac following treatment with a histone acetyltransferase
885 inhibitor (25 µM JG2016) or histone deacetylase inhibitor (0.5 µM Vorinostat) in the presence or
886 absence of 1 mM DFMO. Cells (10T1/2 or SK-N-BE(2)) were pre-treated with DFMO for 24 hours and
887 then transferred into media with HAT and HDAC inhibitors with or without DFMO for 24 hours.
888 C) Western blot showing H3K9me2 abundance following *in vitro* methyl-transferase reaction by G9a.
889 Recombinant G9a was incubated in the presence of recombinant K9me2-modified mononucleosomes
890 and 100 µM putrescine, spermidine, or spermine for one hour at 37°C. Reaction was quenched with
891 SDS, boiled, and assessed by western blot.
892 D) *In vitro* methyl-transferase reactions with G9a and nucleosome as per C) incubated in charge-matched
893 concentrations of putrescine, spermidine and spermine.
894 E) *In vitro* methyl-transferase reactions with G9a and histone H3 incubated in charge-matched
895 concentrations of putrescine, spermidine and spermine.
896 F) Western blot showing H3K9ac abundance following *in vitro* acetyl-transferase reaction with
897 recombinant Gcn5, mononucleosomes and indicated polyamine species. Reactions were incubated for
898 one hour at 37°C, and quenched with SDS.

899 G) Western blot showing H3K9me2 abundance following *in vitro* demethylation reaction. Recombinant
900 Kdm4a was incubated in the presence of recombinant H3K9me2 mononucleosomes and 100 µM
901 putrescine, spermidine, or spermine for two hours at 37°C.
902 H) Western blot showing H318ac abundance following *in vitro* deacetylation reactions. Recombinant Sirt6
903 was incubated with recombinant acetylated nucleosomes and 100 µM putrescine, spermidine, or
904 spermine for one hour at 37°C.
905
906 **Figure 5**
907 A) Time-course of trypsin-digestion of nucleosome substrate in the presence or absence of 100 µM
908 spermidine visualized by Imperial stain of SDS-page-separated samples.
909 B) Time-course of trypsin-digestion of nucleosome substrate in the presence or absence of 100 µM
910 spermine visualized by Imperial stain of SDS-page-separated samples.
911 C) Overlay of the selected regions in the ^{1}H, ^{15}N-HSQC spectra of ^{15}N-H3-NCP (128 µM) with (dark blue)
912 and without (light blue) 512 µM spermidine trichloride (left) and with (green) and without (grey) 512 µM
913 spermine trichloride.
914 D) Top) Normalized chemical shift difference as a function of H3 tail residues in ^{15}N-H3-NCP at 512 µM
915 spermidine (left) or spermine (right) trichloride concentration. The dotted line represents the average
916 shift. Bottom) Rotational correlation time (τ_C) of H3 tail residues in ^{15}N-H3-NCP with (dark blue/green)
917 and without (dark blue/green) spermidine/spermine.
918
919 **Figure 6**
920 A) Mouse embryonic fibroblasts expressing GFP under the control of the endogenous Oct4 locus were
921 reprogrammed with either three (Oct4, Sox2, Klf4; OSK), or four (Oct4, Sox2, Klf4, Myc; OSKM)
922 Yamanaka factors.

923 B) Top: timeline of reprogramming experiments: MEFs were plated on a feeder layer and treated with
924 doxycycline to induce OSK and OSKM expression. Doxycycline was removed at day 12 and doxycycline-
925 independent colonies assessed after four days. Bottom: Oct4-GFP expression quantified by flow
926 cytometry of indicated cells.
927 C) Morphology and Oct4-GFP expression of reprogrammed colonies following the indicated treatments.
928 Scale bars are 275 µM.
929 D) Reprogramming efficiency quantified by calculating the number of Oct4-GFP-positive colonies
930 following indicated treatments as a percentage of initial cells plated. Each data point represents one
931 biological replicate. P values correspond to Tukey's test.
932 E) Reprogramming efficiency of OSKM cells treated with indicated compounds and quantified as per D). P
933 values correspond to Tukey's test. HATi: histone acetyl-transferase inhibitor A-485 0.5 µM.
934 F) Model of effects of polyamines on accessibility of histone tail (H3 tail highlighted).
935

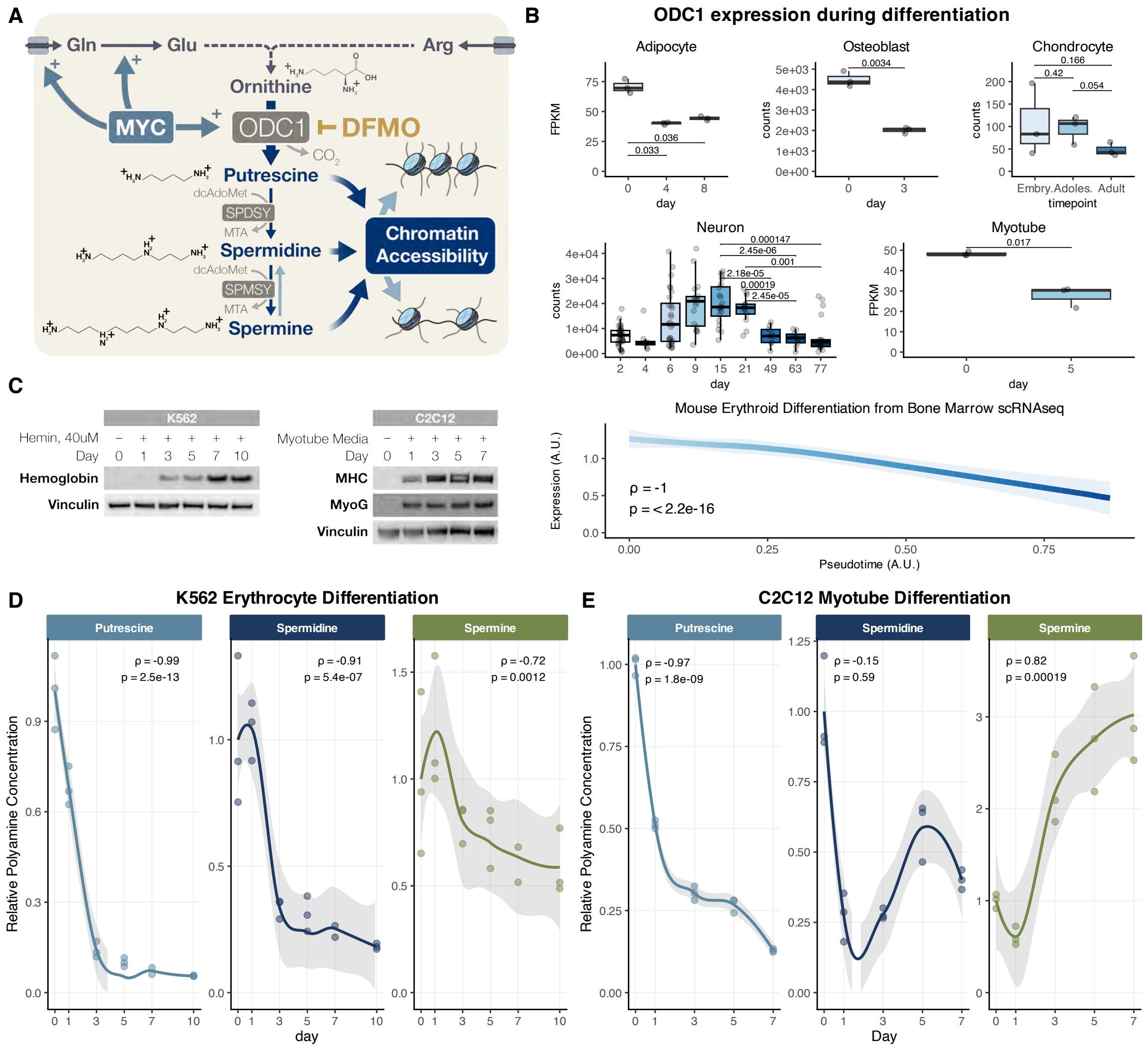
A
Gln
Glu
Arg
Ornithine
MYC
ODC1
DFMO
CO2
Putrescine
dcAdoMet
SPDSY
MTA
Spermidine
dcAdoMet
SPMSY
MTA
Spermine
Chromatin Accessibility
B
ODC1 expression during differentiation
Adipocyte
FPKM
day
0.036
0.033
Osteoblast
counts
day
0.0034
Chondrocyte
counts
timepoint
Embry. Adoles. Adult
0.166
0.42
0.054
Neuron
counts
day
0.000147
2.45e-06
0.001
2.18e-05
0.00019
2.45e-05
Myotube
FPKM
day
0.017
C
K562
Hemin, 40uM
Day
Hemoglobin
Vinculin
C2C12
Myotube Media
Day
MHC
MyoG
Vinculin
Mouse Erythroid Differentiation from Bone Marrow scRNAseq
Expression (A.U.)
ρ = -1
p = < 2.2e-16
Pseudotime (A.U.)
D
K562 Erythrocyte Differentiation
Putrescine
ρ = -0.99
p = 2.5e-13
Spermidine
ρ = -0.91
p = 5.4e-07
Spermine
ρ = -0.72
p = 0.0012
Relative Polyamine Concentration
day
E
C2C12 Myotube Differentiation
Putrescine
ρ = -0.97
p = 1.8e-09
Spermidine
ρ = -0.15
p = 0.59
Spermine
ρ = 0.82
p = 0.00019
Relative Polyamine Concentration
Day

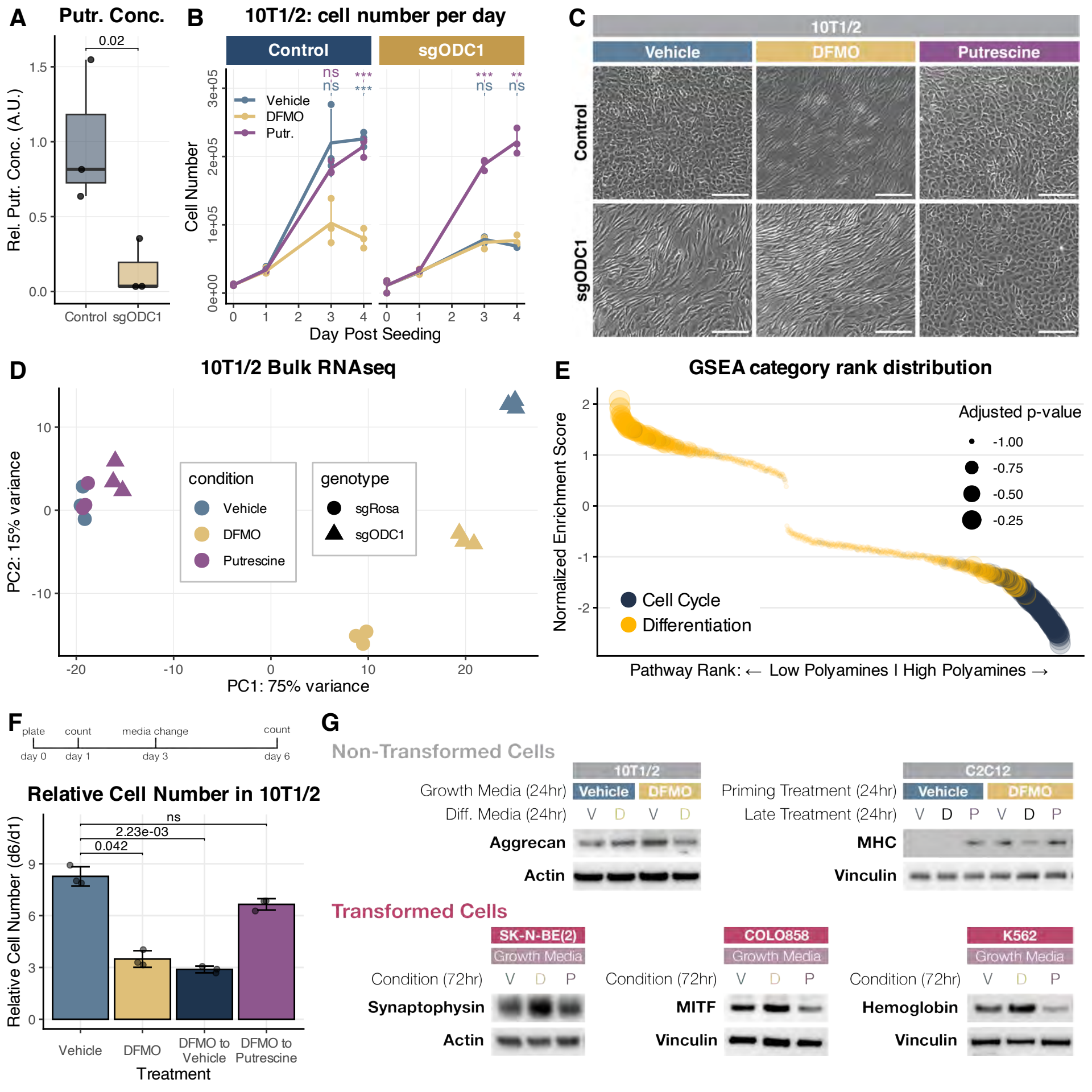
A
Putr. Conc.
0.02
Rel. Putr. Conc. (A.U.)
1.5
1.0
0.5
0.0
Control
sgODC1
B
10T1/2: cell number per day
Control
sgODC1
Vehicle
DFMO
Putr.
ns
n's
***
Cell Number
3e+05
2e+05
1e+05
0e+00
0
1
2
3
4
Day Post Seeding
C
10T1/2
Vehicle
DFMO
Putrescine
Control
sgODC1
D
10T1/2 Bulk RNAseq
PC2: 15% variance
PC1: 75% variance
condition
Vehicle
DFMO
Putrescine
genotype
sgRosa
sgODC1
10
0
-10
-20
20
E
GSEA category rank distribution
Normalized Enrichment Score
Adjusted p-value
-1.00
-0.75
-0.50
-0.25
Cell Cycle
Differentiation
Pathway Rank: ← Low Polyamines | High Polyamines →
2
1
0
-1
-2
F
plate
count
media change
count
day 0
day 1
day 3
day 6
Relative Cell Number in 10T1/2
Relative Cell Number (d6/d1)
ns
2.23e-03
0.042
9
6
3
0
Vehicle
DFMO
DFMO to Vehicle
DFMO to Putrescine
Treatment
G
Non-Transformed Cells
10T1/2
Growth Media (24hr)
Vehicle
DFMO
Diff. Media (24hr)
V
D
Aggrecan
Actin
C2C12
Priming Treatment (24hr)
Late Treatment (24hr)
P
MHC
Vinculin
Transformed Cells
SK-N-BE(2)
COLO858
K562
Growth Media
Condition (72hr)
Synaptophysin
MITF
Hemoglobin

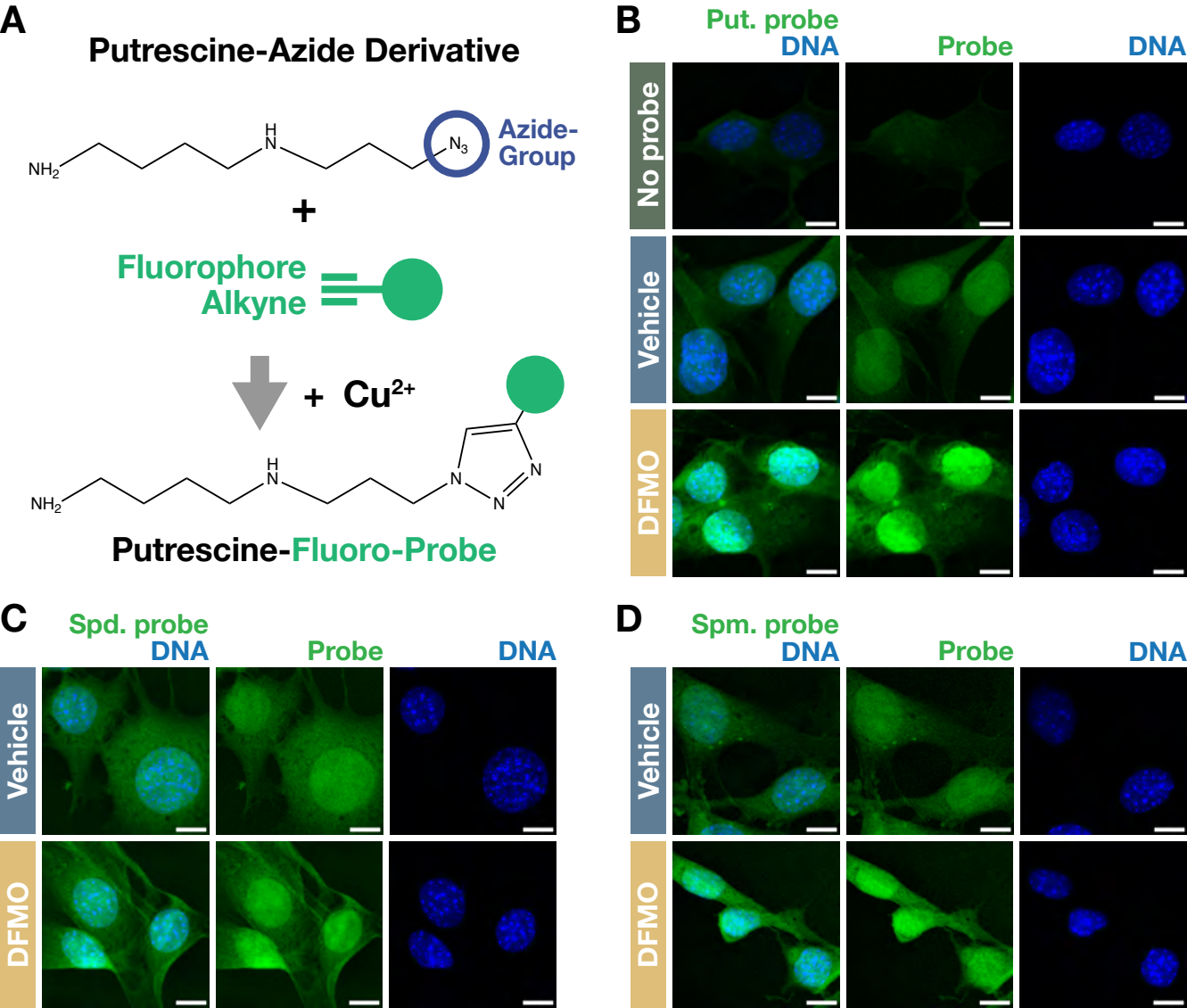
A
Putrescine-Azide Derivative
NH2
H
N
N3
Azide-
Group
+
Fluorophore
Alkyne
+ Cu2+
NH2
H
N
N
N
N
Putrescine-Fluoro-Probe
B
Put. probe
DNA
Probe
DNA
No probe
Vehicle
DFMO
C
Spd. probe
DNA
Probe
DNA
Vehicle
DFMO
D
Spm. probe
DNA
Probe
DNA
Vehicle
DFMO

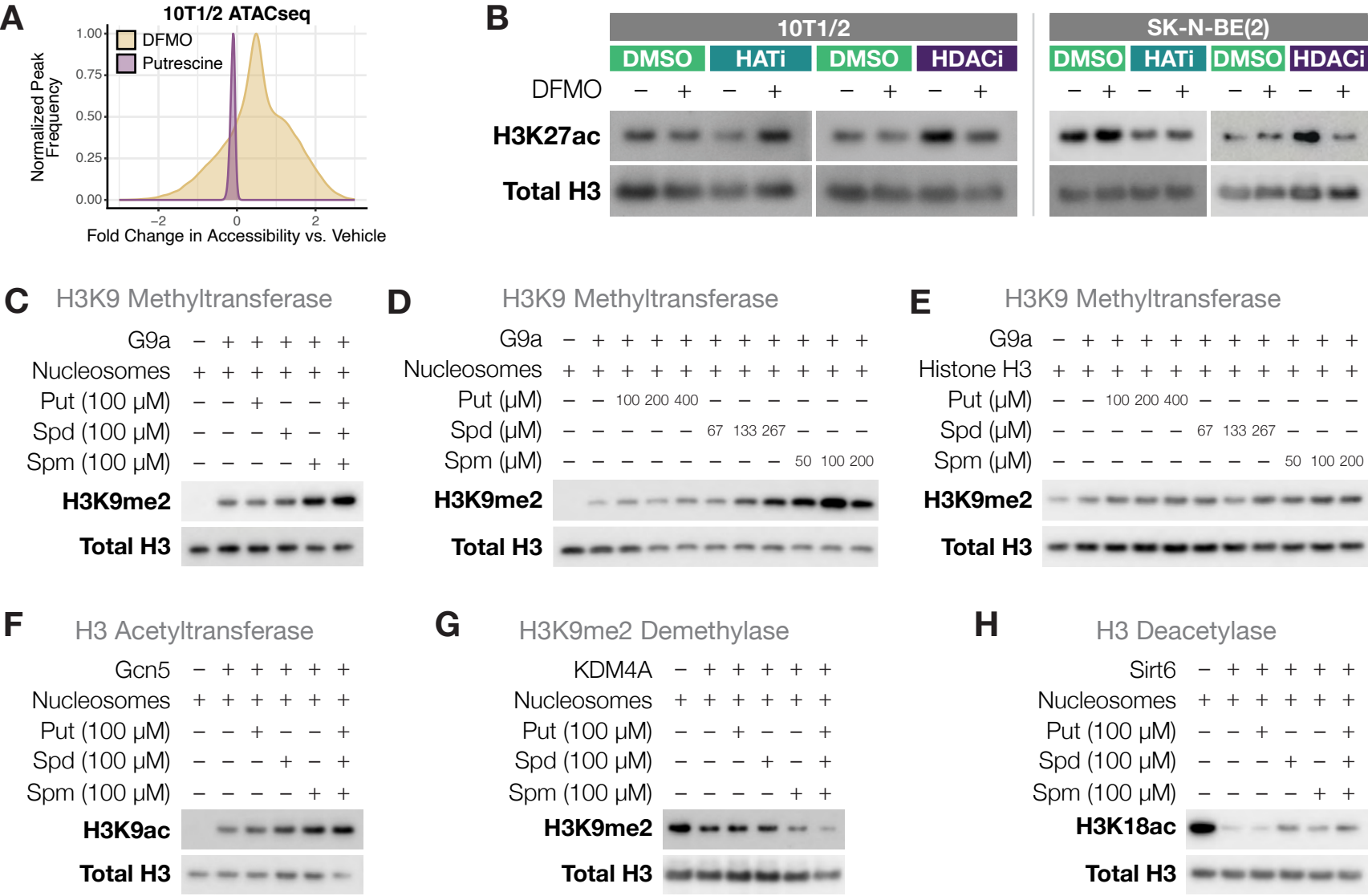
A
10T1/2 ATACseq
DFMO
Putrescine
Normalized Peak Frequency
1.00
0.75
0.50
0.25
0.00
−2
0
2
Fold Change in Accessibility vs. Vehicle
B
10T1/2
SK-N-BE(2)
DMSO
HATi
DMSO
HDACi
DMSO
HATi
DMSO
HDACi
DFMO
H3K27ac
Total H3
C
H3K9 Methyltransferase
G9a
Nucleosomes
Put (100 μM)
Spd (100 μM)
Spm (100 μM)
H3K9me2
Total H3
D
H3K9 Methyltransferase
G9a
Nucleosomes
Put (μM)
Spd (μM)
Spm (μM)
100 200 400
67 133 267
50 100 200
H3K9me2
Total H3
E
H3K9 Methyltransferase
G9a
Histone H3
Put (μM)
Spd (μM)
Spm (μM)
100 200 400
67 133 267
50 100 200
H3K9me2
Total H3
F
H3 Acetyltransferase
Gcn5
Nucleosomes
Put (100 μM)
Spd (100 μM)
Spm (100 μM)
H3K9ac
Total H3
G
H3K9me2 Demethylase
KDM4A
Nucleosomes
Put (100 μM)
Spd (100 μM)
Spm (100 μM)
H3K9me2
Total H3
H
H3 Deacetylase
Sirt6
Nucleosomes
Put (100 μM)
Spd (100 μM)
Spm (100 μM)
H3K18ac
Total H3

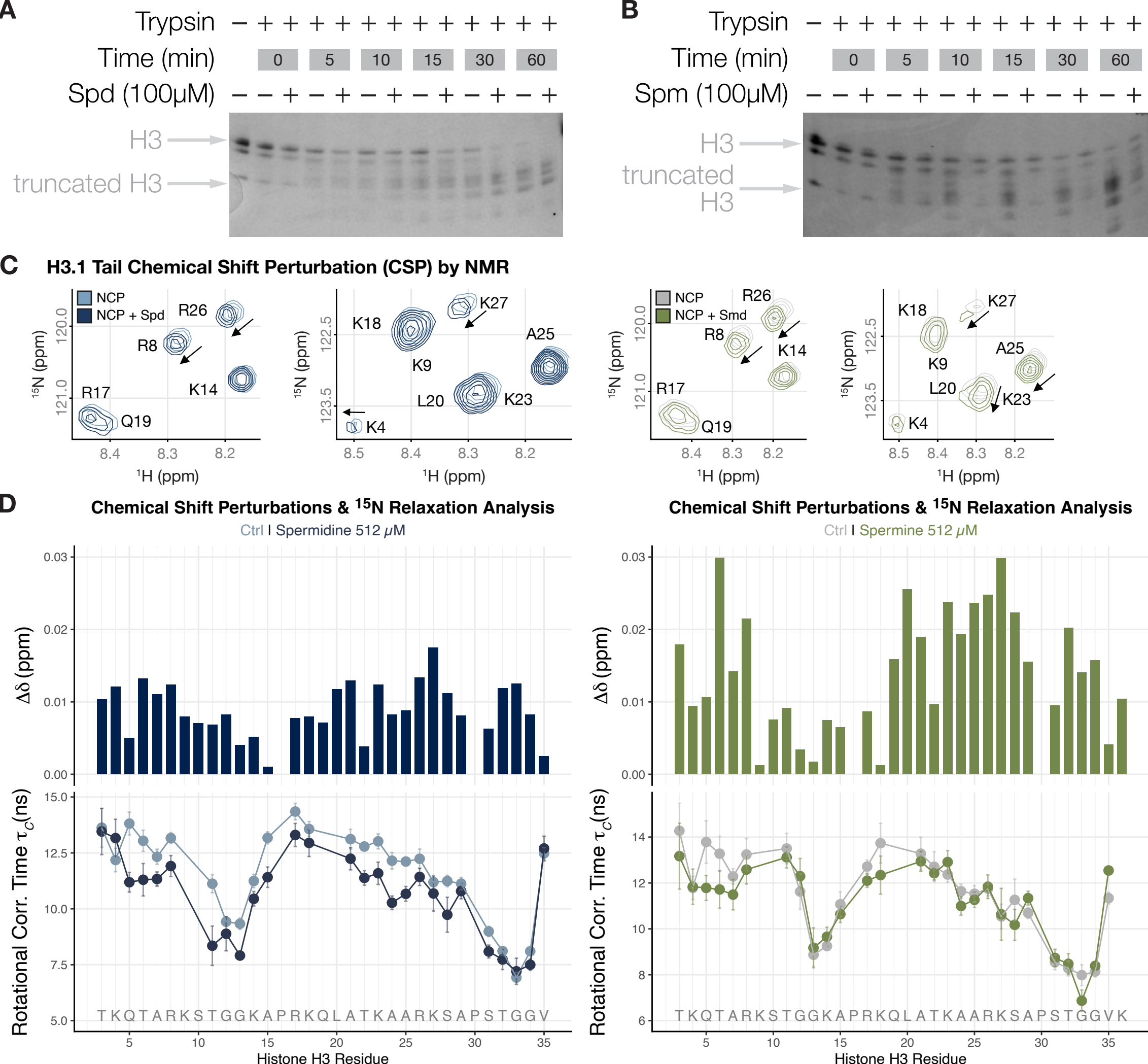
A
Trypsin
Time (min)
0 5 10 15 30 60
Spd (100μM)
H3
truncated H3
B
Trypsin
Time (min)
0 5 10 15 30 60
Spm (100μM)
H3
truncated H3
C
H3.1 Tail Chemical Shift Perturbation (CSP) by NMR
NCP
NCP + Spd
NCP + Smd
R26
R8
K14
R17
Q19
K18
K27
K9
A25
L20
K23
K4
^{15}N (ppm)
^{1}H (ppm)
D
Chemical Shift Perturbations & ^{15}N Relaxation Analysis
Ctrl | Spermidine 512 μM
Ctrl | Spermine 512 μM
Δδ (ppm)
Rotational Corr. Time τ_C(ns)
T K Q T A R K S T G G K A P R K Q L A T K A A R K S A P S T G G V
T K Q T A R K S T G G K A P R K Q L A T K A A R K S A P S T G G V K
Histone H3 Residue

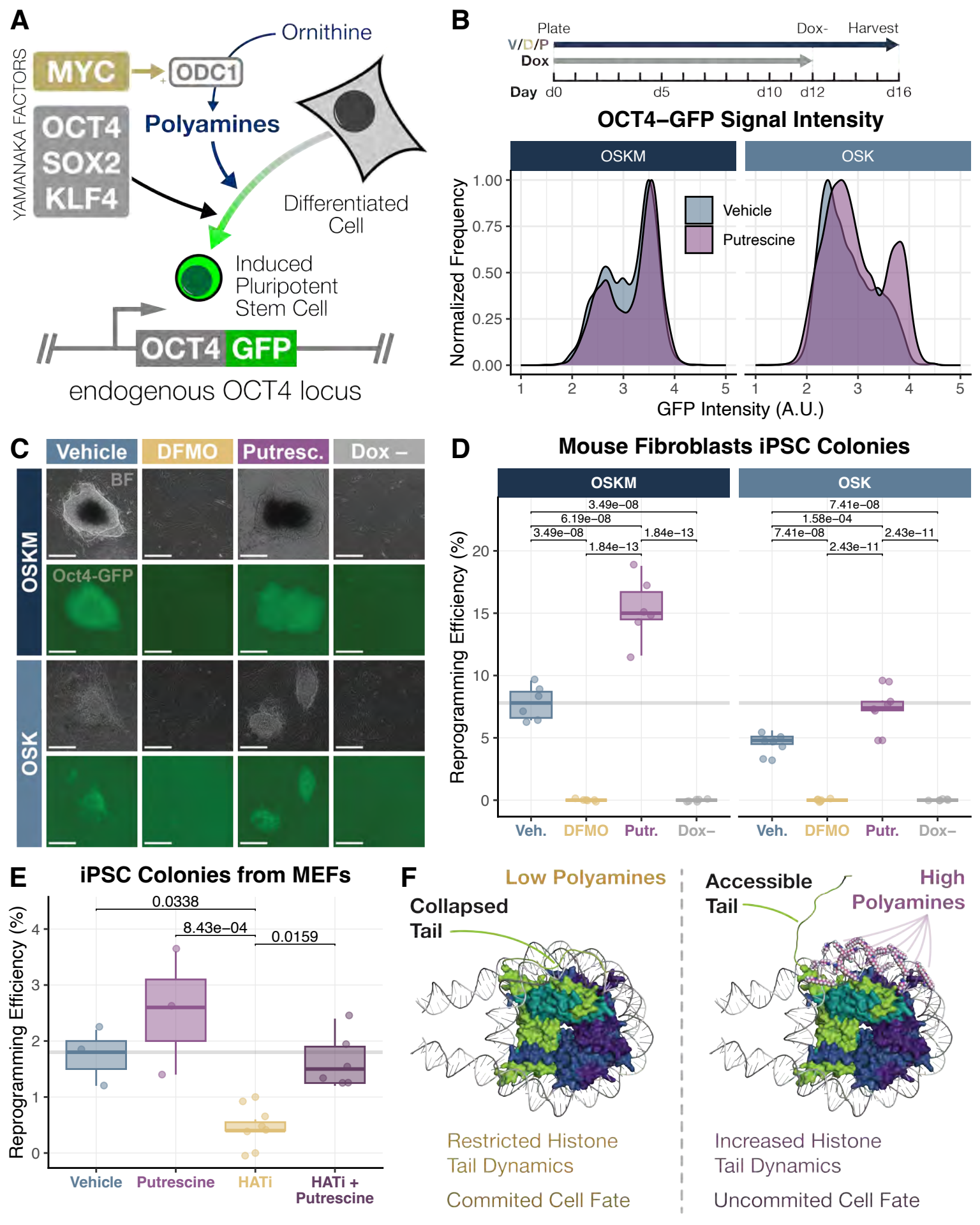
A
YAMANAKA FACTORS
MYC
ODC1
Ornithine
OCT4
SOX2
KLF4
Polyamines
Differentiated Cell
Induced Pluripotent Stem Cell
OCT4
GFP
endogenous OCT4 locus
B
Plate
Dox-
Harvest
V/D/P
Dox
Day d0 d5 d10 d12 d16
OCT4–GFP Signal Intensity
OSKM
OSK
Vehicle
Putrescine
Normalized Frequency
GFP Intensity (A.U.)
C
Vehicle
DFMO
Putresc.
Dox –
BF
Oct4-GFP
OSKM
OSK
D
Mouse Fibroblasts iPSC Colonies
OSKM
OSK
Reprogramming Efficiency (%)
3.49e−08
6.19e−08
3.49e−08
1.84e−13
1.84e−13
7.41e−08
1.58e−04
7.41e−08
2.43e−11
2.43e−11
Veh.
DFMO
Putr.
Dox–
E
iPSC Colonies from MEFs
Reprogramming Efficiency (%)
0.0338
8.43e−04
0.0159
Vehicle
Putrescine
HATi
HATi + Putrescine
F
Low Polyamines
Collapsed Tail
Restricted Histone Tail Dynamics
Commited Cell Fate
Accessible Tail
High Polyamines
Increased Histone Tail Dynamics
Uncommited Cell Fate